JGR Solid Earth

RESEARCH ARTICLE
10.1029/2023JB027679

Seismic Anisotropy of Mafic Blueschists: EBSD-Based Constraints From the Exhumed Rock Record

Jason N. Ott[1], Cailey B. Condit[1], Vera Schulte-Pelkum[2], Rachel Bernard[3], and Matej Pec[4]

[1]Department of Earth and Space Sciences, University of Washington, Seattle, WA, USA, [2]Cooperative Institute for Research in Environmental Sciences and Department of Geological Sciences, University of Colorado, Boulder, CO, USA, [3]Geology Department, Amherst College, Amherst, MA, USA, [4]Department of Earth, Atmospheric and Planetary Sciences, Massachusetts Institute of Technology, Cambridge, MA, USA

Key Points:

- Calculated blueschist Vp anisotropy up to ~20% with a plateau at ~10%, with lineation-parallel fast axis and foliation-normal slow axis
- The anisotropy magnitude increases with glaucophane modal abundance/crystallographic preferred orientation (CPO) strength and is diluted by epidote/lawsonite abundance
- The glaucophane CPO type correlates with the Vp pattern and increasing AVp magnitude in mafic blueschists

Supporting Information:

Supporting Information may be found in the online version of this article.

Correspondence to:

J. N. Ott,
jasonott@uw.edu

Citation:

Ott, J. N., Condit, C. B., Schulte-Pelkum, V., Bernard, R., & Pec, M. (2024). Seismic anisotropy of mafic blueschists: EBSD-based constraints from the exhumed rock record. *Journal of Geophysical Research: Solid Earth*, *129*, e2023JB027679. https://doi.org/10.1029/2023JB027679

Received 14 AUG 2023
Accepted 26 JAN 2024

Author Contributions:

Conceptualization: Jason N. Ott, Cailey B. Condit
Data curation: Jason N. Ott
Formal analysis: Jason N. Ott, Cailey B. Condit
Funding acquisition: Cailey B. Condit
Investigation: Jason N. Ott, Cailey B. Condit
Methodology: Jason N. Ott, Cailey B. Condit
Project administration: Cailey B. Condit
Resources: Jason N. Ott, Cailey B. Condit
Supervision: Cailey B. Condit
Validation: Jason N. Ott
Visualization: Jason N. Ott, Cailey B. Condit, Matej Pec

Abstract Seismic anisotropy constitutes a useful tool for imaging the structure along the plate interface in subduction zones, but the seismic properties of mafic blueschists, a common rock type in subduction zones, remain poorly constrained. We applied the technique of electron backscatter diffraction (EBSD) based petrofabric analysis to calculate the seismic anisotropies of 14 naturally deformed mafic blueschists at dry, ambient conditions. The ductilely deformed blueschists were collected from terranes with inferred peak P-T conditions applicable to subducting slabs at or near the plate interface in active subduction zones. Epidote blueschists display the greatest *P* wave anisotropy range (AVp ~7%–20%), while lawsonite blueschist AVp ranges from ~2% to 10%. *S* wave anisotropies generate shear wave splitting delay times up to ~0.1 s over a thickness of 5 km. AVp magnitude increases with glaucophane abundance (from areal EBSD measurements), decreases with increasing epidote or lawsonite abundance, and is enhanced by glaucophane crystallographic preferred orientation (CPO) strength. Two-phase rock recipe models provide further evidence of the primary role of glaucophane, epidote, and lawsonite in generating blueschist seismic anisotropy. The symmetry of *P* wave velocity patterns reflects the deformation-induced CPO type in glaucophane—an effect previously observed for hornblende on amphibolite *P* wave anisotropy. The distinctive seismic properties that distinguish blueschist from other subduction zone rock types and the strong correlation between anisotropy magnitude/symmetry and glaucophane CPO suggest that seismic anisotropy may be a useful tool in mapping the extent and deformation of blueschists along the interface, and the blueschist-eclogite transition in active subduction zones.

Plain Language Summary The directional dependence of seismic wave speeds in the subsurface, or seismic anisotropy, can allow us to map the Earth's structure in subduction zones. To improve the interpretation of seismic data collected in active subduction zones, we characterized the range of seismic anisotropy created by blueschists (a common subduction zone rock-type) that were returned to the surface after being deformed in ancient subduction margins. We calculate the anisotropy of each blueschist rock from mineral orientations collected in the lab combined with the elastic properties of these minerals. Trends in seismic anisotropy were compared to the changes in composition and preferred orientations of minerals (produced by deformation). We found that blueschists can generate a broad range of seismic anisotropy, and that this anisotropy is enhanced by increasing amounts of the mineral glaucophane. The seismic anisotropy is further increased when the glaucophane minerals are more uniformly oriented, as is typical in rocks that have experienced higher levels of deformation. The seismic anisotropy and seismic wave speeds of blueschists are distinctive from those of other common subduction zone rocks. Therefore, these results suggest blueschist seismic anisotropy can be used to improve our ability to map structure and deformation occurring in active subduction zones.

1. Introduction

Subduction zones are complex convergent boundaries where the majority of deformation between two plates is accommodated by periodic, frictional slip in the shallow seismogenic zone, and aseismic, viscous creep at greater depths (Hyndman et al., 1997). This viscous deformation, localized along the plate interface in ductile shear zones with a thickness of up to a few kilometers (Stöckhert, 2002), plays an important role in transferring stress to the seismogenic zone and generating megathrust earthquakes (Wech & Creager, 2011). The transition from brittle to ductile deformation occurs around the same region as the onset of blueschist facies metamorphism in most active subduction zones (Figures 1a and 1b; Peacock, 2004; van Keken et al., 2018). Observations of exhumed subduction terranes indicate that the thickness of blueschist-metamorphosed oceanic crust at the subduction interface

Writing – original draft: Jason N. Ott, Cailey B. Condit, Vera Schulte-Pelkum, Rachel Bernard, Matej Pec
Writing – review & editing: Jason N. Ott, Cailey B. Condit, Vera Schulte-Pelkum, Rachel Bernard, Matej Pec

can vary from tens of meters to >1 km scales (e.g., Aoki et al., 2008; Brothers, 1974; Lamont et al., 2020; Peillod et al., 2021; Topuz et al., 2008). Deep subduction of mafic blueschist (>70 km) induces a transformation to eclogite through dehydration reactions that release mineral-bound water to enable flux-melting in the overlying mantle-wedge, and arc-volcanism at the surface (Peacock, 1993). Consequently, subducting blueschist-metamorphosed oceanic crust is strongly tied to a range of the mechanical and chemical processes in subduction zones (Figure 1a), yet cannot be studied in situ within active systems. However, we can use geophysical observations of the directional dependence of seismic wave velocities, or seismic anisotropy, in active subduction zones to interpret subsurface structure by constraining the range of seismic anisotropy from exhumed subduction exposures and samples (e.g., Brownlee et al., 2017; Schulte-Pelkum et al., 2005; Schulte-Pelkum & Mahan, 2014a, 2014b).

Seismic anisotropy is produced in large part by crystallographic preferred orientation (CPO) of anisotropic minerals at depths below the closure of open cracks (Almqvist & Mainprice, 2017; Brownlee et al., 2017; Jung, 2017; Mainprice & Humbert, 1994; Mainprice & Nicolas, 1989). CPO formation is typical of the viscous deformation that occurs along the plate interface below the seismogenic zone (Mainprice & Nicolas, 1989), and thus, parts of the subducting slab may develop significant seismic anisotropy if CPOs are developed in anisotropic phases such as amphibole or mica. Seismology-based studies of subduction zones document evidence of seismic anisotropy including azimuthal anisotropy of *P* wave velocities and observations of shear wave splitting between the fast (Vs_1) and slow (Vs_2) shear waves (e.g., Huang et al., 2011; Nakajima & Hasegawa, 2004; Park & Levin, 2002; Wang & Zhao, 2010; Wei et al., 2016). These studies have proposed various source regions for the observed seismic anisotropy including the subducting slab, the underlying subducting mantle lithosphere, and serpentinized mantle wedge. However, in order to understand the relative contributions of these structural units to the overall seismic anisotropy of subduction zones, we need geologic constraints from the rock record that inform us about the range of potential anisotropies and the contribution of the constituent phases and their orientation in producing these seismic signatures.

Some previous investigations have characterized the seismic anisotropy of mafic blueschists using petrofabrics and laboratory velocity measurements (Bezacier et al., 2010; Cao et al., 2013, 2014; Cao & Jung, 2016; Fujimoto et al., 2010; Ha et al., 2019; Keppler et al., 2017; Kim et al., 2013; Park & Jung, 2022; Zertani et al., 2022). Previous studies calculated the anisotropy of naturally deformed blueschists using petrofabrics determined at ambient conditions with electron backscatter diffraction (EBSD) data and the elastic properties of the constituent minerals, and reported *P* wave anisotropies (AVp) from ∼8% to 30%, and maximum *S* wave anisotropies (AVs) from 4% to 24% (Bezacier et al., 2010; Cao et al., 2013, 2014; Cao & Jung, 2016; Ha et al., 2019; Kim et al., 2013). Keppler et al. (2017) calculated the anisotropy of two exhumed blueschists using the elastic properties of the minerals and petrofabrics determined by neutron diffraction at ambient conditions, and reported AVp values ∼7%–12%. In an experimental study, Park and Jung (2022) deformed blueschists under shear in a modified Griggs apparatus at high pressures and temperatures, and calculated anisotropies of AVp ∼5%–11% and max AVs ∼4%–6% using the EBSD-determined petrofabrics of the recovered samples (at ambient conditions). Two studies using ultrasonic measurements of mafic blueschist petrophysical properties at high pressures and temperatures report anisotropies up to AVp ∼13% (Fujimoto et al., 2010), and AVp and max AVs ∼11% (Zertani et al., 2022). Taken together, these studies suggest that blueschist-facies rocks may contribute substantially to the seismic anisotropy observed in active subduction zones by generating *P* wave anisotropies up to 30% and shear wave splitting delay times of up to ∼0.3 s (Cao et al., 2013, 2014; Kim et al., 2013). Most previous investigations include only a few blueschists, or blueschists from a single exhumed subduction terrane. Thus, further work to characterize variations in the potential contribution of blueschists to observed seismic anisotropy in subduction zones by investigating elastic anisotropy in blueschists from different exhumed subduction terranes and peak P-T conditions will be invaluable.

Blueschist facies metamorphism of mid-ocean ridge basaltic crust produces blueschists with variable mineralogies (e.g., lawsonite blueschist or epidote blueschist subtypes; Evans, 1990) depending on the pressure-temperature gradient of the subduction path. Lawsonite blueschists are produced by metamorphism at low temperatures and remain stable to high pressures, while epidote blueschists are the product of metamorphism at warmer temperatures and moderate pressures (Figure 1b). Consequently, exhumed lawsonite blueschists and epidote blueschists preserve evidence of the deformation history of these rocks to the peak P-T conditions they experienced during subduction. The seismic anisotropy generated by both blueschist subtypes can be substantial, although the magnitude of lawsonite blueschist anisotropy is generally observed to be weaker than the anisotropy

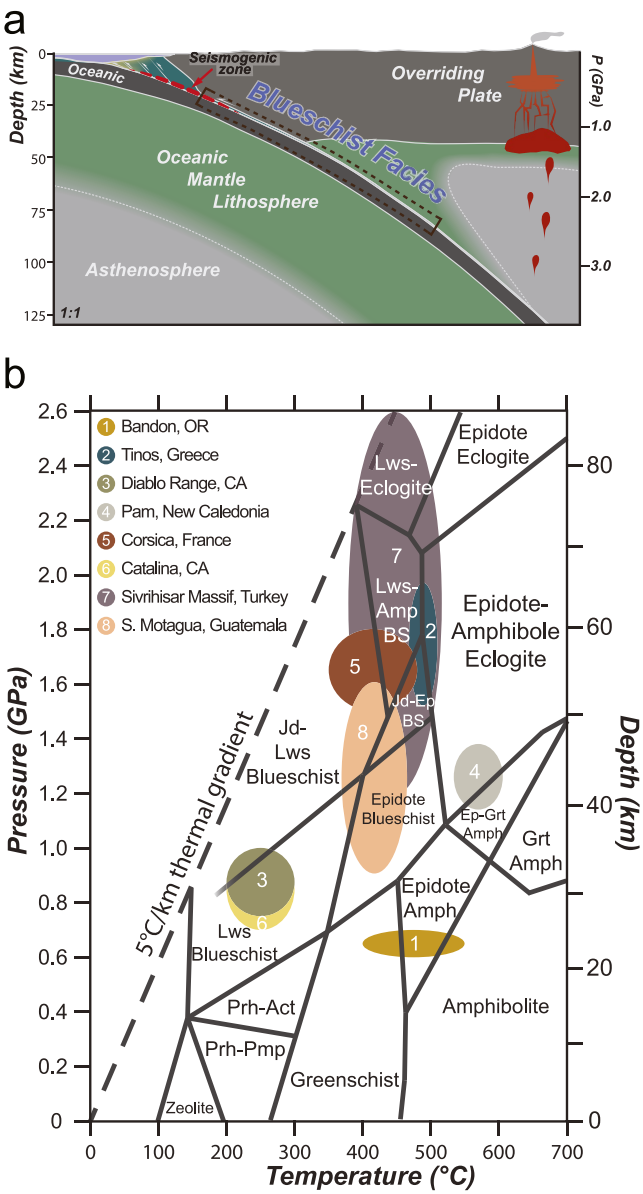

Figure 1. (a) Subduction zone schematic showing distribution of blueschist facies rocks. (b) Pressure-temperature conditions of blueschist samples. Facies boundaries from Peacock (2009). Mineral abbreviations after Whitney and Evans (2010) used in metamorphic facies designations (b): Act = actinolite, Amp = amphibole, Ep = epidote, Grt = garnet, Jd = jadeite, Lws = lawsonite, Prh = prehnite, Pmp = pumpellyite; rock type abbreviations used in metamorphic facies designations (b): BS = blueschist; Ecl = eclogite; Amph = amphibolite.

generated by epidote blueschist (e.g., Fujimoto et al., 2010; Kim et al., 2013). Mafic blueschists are primarily composed of the sodic amphibole glaucophane with significant fractions of epidote (epidote blueschist), lawsonite (lawsonite blueschist), and smaller fractions (<10%) of phengite, garnet, and other accessory phases. Single-crystal elastic wave velocity measurements in multiple crystallographic directions have been made using Brillouin spectroscopy to determine elastic moduli of glaucophane (Bezacier et al., 2010), lawsonite (Schilling et al., 2003), epidote (Aleksandrov et al., 1974), and phengite (muscovite, Vaughan & Guggenheim, 1986). The experimentally determined elastic anisotropies of these phases demonstrate that each may contribute substantially to observed seismic anisotropies (Figures 2a and 2b).

Other amphiboles, such as the hornblende group, and micas (biotite and muscovite) have been proposed as fundamental contributors to the seismic anisotropy of deep crustal (continental) rocks in texture-based seismic anisotropy studies of rocks from the middle and lower continental crust (e.g., Lloyd et al., 2011; Mahan, 2006; Tatham et al., 2008). Amphibole in naturally deformed rocks has been observed with four different CPO types which were proposed to correlate with the deformation conditions experienced (Kim & Jung, 2019; Ko & Jung, 2015). The type-I amphibole CPO is defined by strong alignment of the [100] crystallographic axes subnormal to the shear plane and the [001] axes subparallel to the shear direction, while the type-II CPO shows the same [100] axes orientation with the [010] axes aligned subparallel to the shear direction (Figure 2c). The type-III CPO of amphibole is also characterized by strong alignment of the [100] axes subnormal to the shear plane, but the [010] and [001] axes describe a girdle on the shear plane (Figure 2c). Amphibole with a type-IV CPO displays a strong alignment of the [001] axes subparallel to the shear direction with the [100] and [010] axes describing a girdle subnormal to the shear direction (Figure 2c). Laboratory deformation experiments on amphibolites yielded correlations between amphibole CPO type and the magnitude of seismic anisotropy predicted in the samples (Kim & Jung, 2019, 2020), and studies of naturally deformed amphibolites reported further correlations between the amphibole CPO type and the symmetry of the Vp anisotropy patterns (Ji et al., 2013; Kim & Jung, 2020; Liu & Cao, 2023). In contrast, the contribution of glaucophane to the seismic properties of mafic blueschists is not as well understood due to the limited number of petrofabric based seismic anisotropy studies on mafic blueschists, and the potential contribution of other anisotropic phases to the bulk anisotropy (e.g., epidote, lawsonite, and phengite).

Here, we extend and build up this previous work by creating a catalog of EBSD derived seismic anisotropies for 14 mafic epidote and lawsonite blueschists spanning a large range of P-T conditions from eight exhumed subduction terranes (Figure 1b). We use the EBSD based approach to calculate seismic anisotropy at dry, ambient conditions, which combines measured CPOs, modal abundances derived from indexed regions of EBSD maps, and the elastic properties of each phase to calculate the elastic anisotropy of the aggregate; these microstructural-based calculations provide constraints on the potential contribution of blueschists to seismic anisotropy (Mainprice et al., 2011, 2015; Mainprice & Humbert, 1994). We then investigated the anisotropy trends with respect to modal abundance, CPO type, and CPO strength for glaucophane, epidote, lawsonite, and phengite within each sample assemblage to assess the contribution of the modal abundance and CPO of each phase to the seismic properties. We leveraged the variability in peak metamorphic conditions across our samples to investigate the potential of a correlation between the magnitude of anisotropy and increasing metamorphic grade due to increasing depth of subduction. We find that glaucophane's influence on blueschist seismic anisotropy is similar to that of previous observations of hornblende group

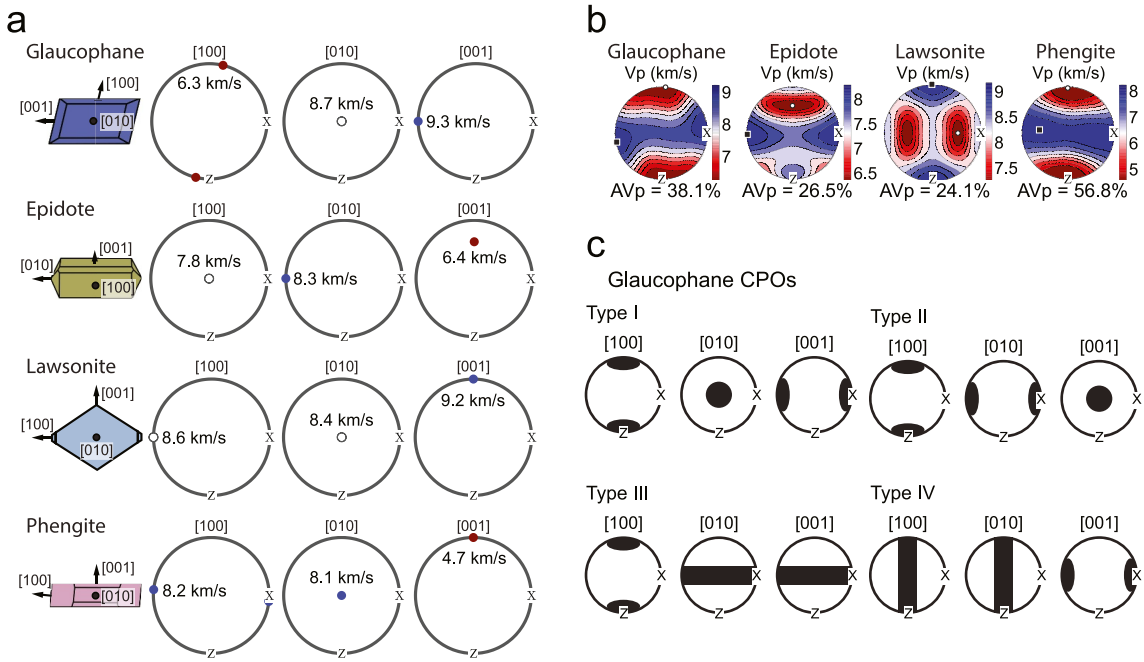

Figure 2. (a) Diagrams of the crystal morphology of glaucophane, epidote, lawsonite, and phengite labeled with the [100], [010], and [001] crystallographic axes in common preferred orientation typical for blueschists in this compilation. Vp velocities of the crystallographic axes on the upper hemisphere stereographic projections (red circles = slow-axis, white circle = intermediate-axis, blue circle = fast-axis). (b) The respective single-crystal Vp seismic velocities projections (upper hemisphere) and seismic anisotropy percentages (AVp) for phases and orientations in panel (a). Black squares and white circles are maximum and minimum *P* wave velocity orientations, respectively. (c) Diagram of crystallographic preferred orientation types previously observed in the amphibole glaucophane in naturally and experimentally deformed samples (modified after Kim & Jung, 2019).

amphiboles on the anisotropy of deep crustal rocks; the modal abundance and CPO strength of the amphibole glaucophane exerts a key control on the magnitude of seismic anisotropy in mafic blueschist and the pattern of *P* wave anisotropy reflects the CPO type of glaucophane.

2. Materials and Methods

2.1. Sample Description and Preparation

We investigated the elastic anisotropy of 14 mafic blueschists covering a wide range of mineralogies, pressure-temperature conditions, and fabrics. This included nine epidote blueschists and five lawsonite blueschists, collected from eight exhumed subduction terranes that experienced peak metamorphic conditions ranging from 200 to 600°C and 0.6–2.6 GPa (Table 1), spanning much of the blueschist facies stability field (Figure 1b). The blueschists were metamorphosed from mafic protoliths and exhibit mineralogies dominantly composed of glaucophane and lawsonite or epidote, with variable amounts of garnet, phengite, pyroxene (jadeite or omphacite), quartz, chlorite, and minor rutile or titanite. Average grain size of the samples ranges from 10 to 80 μm in diameter with some blueschists containing porphyroblasts up to 5 mm in diameter. The samples selected for this study display evidence of ductile deformation, including well-defined foliations and lineations. Photos of hand samples illustrating the macroscopic fabrics are shown in Figure 3.

Thin sections were prepared following the common methodology employed in petrofabric based anisotropy studies (e.g., Brownlee et al., 2017; Cao et al., 2013; Kang & Jung, 2019; Kim et al., 2013; Liu & Cao, 2023; Ward et al., 2012). One structurally oriented thin section, cut parallel to the lineation and perpendicular to the foliation, where the X-Z plane is contained in the thin section, was cut for each sample. Optical microscopy was used to select target regions for EBSD data collection in each thin section that were representative of the mineralogy, grain sizes, and fabric of the full section and hand sample. Examples of selected representative regions and their microstructures are presented in Figure 4 and photomicrographs of larger areas containing the target regions of samples are included in Figure S1 in Supporting Information S1.

Table 1
Samples, Localities, and P-T Estimates

Sample	Locality[a]	P (GPa)	T (°C)	Reference
Epidote blueschist				
BAN09	Bandon, Oregon, USA	0.6–0.7	400–550	Coleman and Lanphere (1971)
BAN15	Bandon, Oregon, USA	0.6–0.7	400–550	Coleman and Lanphere (1971)
CY106	Tinos, Cycladic Islands, Greece	1.52–1.97	468–510	Lamont et al. (2020)
CY107	Tinos, Cycladic Islands, Greece	1.52–1.97	468–510	Lamont et al. (2020)
DR221	Diablo Range, California, USA	0.75–1.0	200–300	Patrick and Day (1989)
LAB34	Diablo Range, California, USA	0.75–1.0	200–300	Patrick and Day (1989)
LAB555	Pam Peninsula, New Caledonia	1.26 ± 0.12	570 ± 36	Clarke et al. (1997)
LAB570	Pam Peninsula, New Caledonia	1.26 ± 0.12	570 ± 36	Clarke et al. (1997)
LAB572	Pam Peninsula, New Caledonia	1.26 ± 0.12	570 ± 36	Clarke et al. (1997)
Lawsonite blueschist				
C18G1003C01	Corsica, France	1.5–1.8	350–480	Brovarone et al. (2014)
DR265	Diablo Range, California, USA	0.75–1.0	200–300	Patrick and Day (1989)
GB15-02A	Catalina Schist, California, USA	0.7–1.0	200–300	Grove and Bebout (1995)
SV01-49A	Sivrihisar Massif, Turkey	1.2–2.6	380–520	Davis and Whitney (2006)
01GSN2-3	S. Motagua Fault Zone, Guatemala	0.9–1.6	370–460	Harlow et al. (2003)

[a]Sample location coordinates are available for samples: C18G1003C01 (42°23′30.4″N 9°19′22.9″E), GB15 (33°22′N 118°28′W), and SV01(39°36′00.7″N 31°15′26.9″E). Remaining sample details are available only for the locality.

2.2. EBSD Data Acquisition

The EBSD technique relies on the interaction of an incident electron beam with a flat sample mounted with the normal vector of the surface oriented at a high angle to the electron beam. The electrons interact with the sample at a shallow depth (~1 μm), and electrons diffracted by the lattice planes of mineral phases in the sample are imaged as bands on the phosphor screen of the EBSD detector. Prior et al. (1999) provides a detailed review of the EBSD technique. Multiple bands are imaged at each indexed point, forming a Kikuchi pattern that can be matched with a crystallographic database to identify the phase and its orientation within the sample (e.g., Britton et al., 2016; Lloyd et al., 1991). Improvements in automated data collection, Kikuchi pattern recognition, and indexing of EBSD data allows for the collection of dense phase-and-orientation data sets over large areas in thin sections prepared from geologic samples, making EBSD a powerful tool for the study of physical properties that are connected to rock microstructures (Krieger Lassen et al., 1992; Prior et al., 1999; Wright, 2000).

EBSD data were collected at the University of Washington Molecular Analysis Facility using a ThermoFisher-Scientific Apreo variable-pressure scanning electron microscope (SEM) equipped with an Oxford Instruments Symmetry EBSD detector. Prior to data collection, samples were polished for 2–6 hr with a 0.06 μm-diameter amorphous, colloidal silica suspension in a Bruker VibroMet 2 vibratory polisher. Samples with an indexing rate less than 75% after a test map were polished for an additional 2 hr before data collection.

EBSD data for 13 of the 14 samples were collected at SEM chamber pressure of 160 Pa with a pressure-limiting apparatus installed on the beam column, resulting in a limited working distance of 18 mm. All samples were mounted to the stage with a fixed 70° tilt, and data was collected at an accelerating voltage of 20 kV and 32 nA current. Sample LAB555 was coated in a 10 nm layer of carbon to dissipate sample charging and run at high-vacuum conditions with no pressure-limiting apparatus and a shorter working distance of 16 mm to improve the indexing rate of this fine grained sample.

EBSD patterns were collected on a grid with a step size selected to optimize sample characterization and collection time. Selected step sizes ranged from 1.5 to 10 μm based on the average observed grain size in the sample, and the exposure time at each step was 20 ms. EBSD-map areas varied from 1.3 mm by 1.7 mm to 3.6 mm by 9.3 mm. The EBSD patterns were indexed using the Oxford HKL and American Mineralogist databases loaded in the Oxford

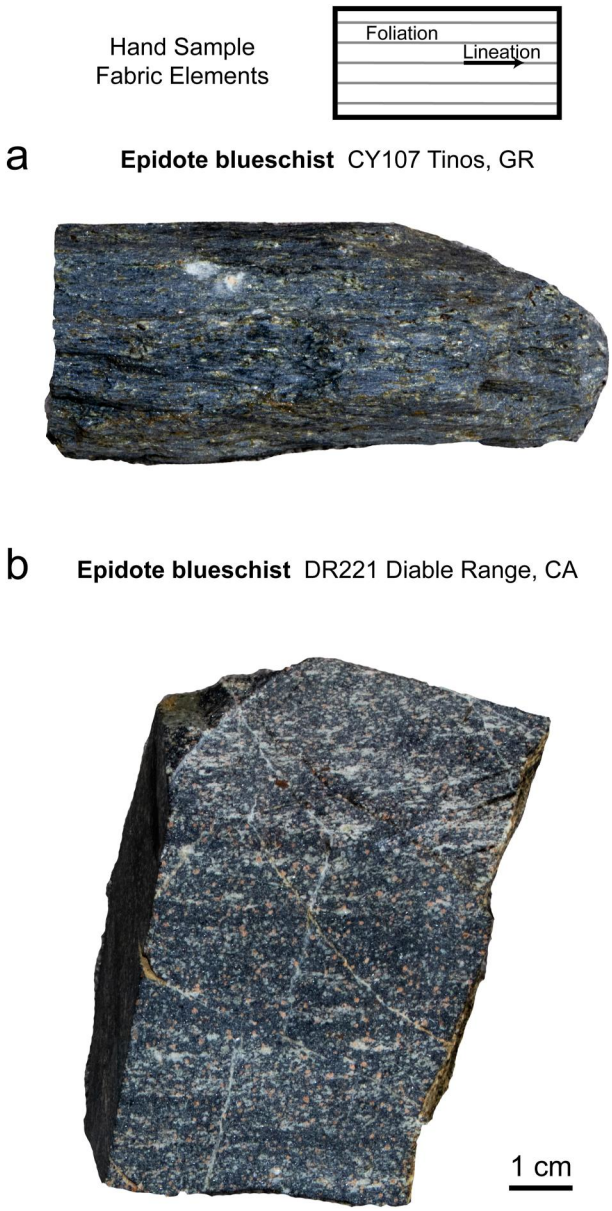

Figure 3. Photos of blueschist hand samples representative of the macroscopic fabrics observed in the samples selected for this study. The approximately horizontal foliation and lineation (subhorizontal in the plane of the page) in the epidote blueschists from (a) Tinos, Greece and (b) the Diablo Range, California is largely defined by the volumetrically dominant elongate glaucophane grains. Scale bar is applicable to both samples.

AZtec software. Inclusion of the jadeite and/or omphacite match units during EBSD data collection and sample indexing was based on the presence of calcium (suggesting omphacite) in qualitative energy-dispersive X-ray spectroscopy on test maps of sample regions containing pyroxene.

2.3. EBSD Data Analysis

Microstructural analysis and calculation of the seismic anisotropy were done with the MTEX 5.7.0 toolbox for MATLAB (Bachmann et al., 2010; Mainprice et al., 2011). Each EBSD map was processed to remove low confidence data with a mean angular deviation greater than 1.0° from the crystallographic database reference data. Grains were reconstructed with a threshold of greater than 10° between neighboring EBSD measurements. We removed grains with fewer than three indexed points. These reduced EBSD data sets were used in all subsequent analyses.

2.3.1. Seismic Anisotropy Calculations

To calculate seismic anisotropy, we combined the quantitative measure of the CPOs from the full set of indexed orientations with published single crystal elastic tensors for the constituent phases (Table 2) to calculate the effective elastic properties of each multiphase crystalline aggregate (Mainprice et al., 2011, 2015; Mainprice & Humbert, 1994). Stress is linked to strain through the general tensor form of Hooke's law as

$$\sigma_{ij} = C_{ijkl}\varepsilon_{kl} \tag{1}$$

where σ_{ij} is the stress tensor, ε_{kl} is the strain tensor and C_{ijkl} is the full elastic stiffness tensor. The elastic stiffness tensor is a fourth-rank tensor with 81 components, but the symmetry of the stress and strain tensors requires that $C_{ijkl} = C_{jikl}$ and $C_{ijkl} = C_{ijlk}$, reducing the number of independent entries to 36. The resultant 6×6 Voigt matrix representation of the elastic stiffness tensor may be further reduced to 21 independent elastic constants due to thermodynamic strain energy conditions that require $C_{ijkl} = C_{klij}$. In this work, we will present the elastic stiffness constants for each phase and the polyphase aggregates in the Voigt matrix representation as

$$C_{IJ} = C_{ijkl} = \begin{vmatrix} C_{11} & C_{12} & C_{13} & C_{14} & C_{15} & C_{16} \\ & C_{22} & C_{23} & C_{24} & C_{25} & C_{26} \\ & & C_{33} & C_{34} & C_{35} & C_{36} \\ & & & C_{44} & C_{45} & C_{46} \\ & & & & C_{55} & C_{56} \\ & & & & & C_{66} \end{vmatrix} \tag{2}$$

A detailed description of the reduction of a full elastic stiffness tensor into its reduced Voigt matrix representation (Voigt stiffness matrix) is included in Almqvist and Mainprice (2017). While grain size, shape, crystallographic orientation, and distribution of phases may be heterogeneous at microscopic scales, we treat the samples as representative of the macroscopic structure and composition and assume that stress and strain vary slowly and continuously with position, and are linked through the effective elastic stiffness tensor, C^* (Mainprice & Humbert, 1994; Mainprice, 2015).

To determine C^* for each phase, the full set of indexed orientations for each phase was fitted in MTEX by an orientation distribution function (ODF)—a mathematical function in spherical harmonics that weighs each

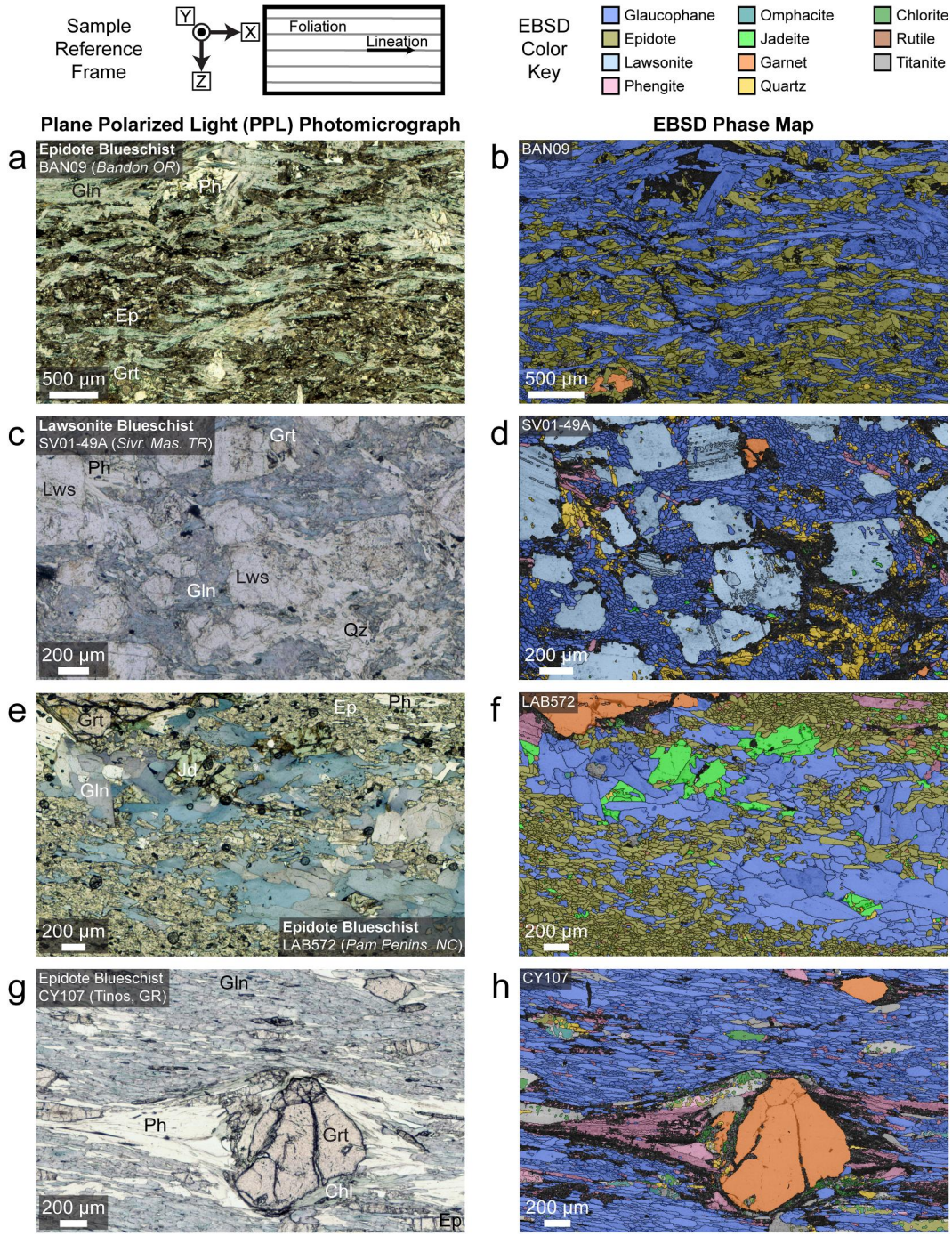

Figure 4. (a, b) Bandon, OR epidote blueschist showing foliation defined by shape preferred orientation of glaucophane and epidote grains; (c, d) Sivrihisar Massif, TUR lawsonite blueschist with lawsonite porphyroblasts in matrix of fine-grained glaucophane; (e, f) epidote blueschist from Pam Peninsula, NC, with foliation defined by compositional layers of fine-grained epidote and large glaucophane grains; (g, h) epidote blueschist from Tinos, GRC, with strong foliation in elongate glaucophane grains and phengite in garnet pressure-shadows.

possible orientation by the fraction of the phase with that orientation (Bunge, 1985). The single crystal Voigt elastic stiffness matrix for each phase (Table 2) were integrated over the ODF in MTEX to calculate the effective elastic Voigt stiffness matrix C^* for each phase using three averaging schemes: (a) the Voigt average that assumes uniform strain throughout the sample (Voigt, 1928), (b) the Reuss average that assumes uniform stress throughout

Journal of Geophysical Research: Solid Earth

10.1029/2023JB027679

Table 2
Referenced Single-Crystal Elastic Constants in Voigt Matrix Notation[a] (in GPa)

Chlorite **(density = 2.54 g/cm^3)**			**Mookherjee and Mainprice (2014)**			***Epidote*** **(density = 3.45 g/cm^3)**			**Aleksandrov et al. (1974)**		
198.4	57.3	14.0	0	3.0	0	211.5	65.6	43.2	0	−6.5	0
	197.7	19.6	0	−0.5	0		239.0	43.6	0	−10.4	0
		138.1	0	0.1	0			202.1	0	−20.0	0
			25.9	0	0.1				39.1	0	−2.3
				24.6	0					43.4	0
					71.0						79.5
Garnet (almandine) (density = 3.8 g/cm^3)			Chai et al. (1997)			*Glaucophane* (density = 3.07 g/cm^3)			Bezacier et al. (2010)		
306.7	106.7	111.9	0	0	0	122.3	46.7	37.2	0	2.3	0
	306.7	111.9	0	0	0		231.5	74.9	0	−4.8	0
		306.7	0	0	0			254.6	0	−23.7	0
			94.9	0	0				79.6	0	8.9
				94.9	0					52.8	0
					94.9						51.2
Jadeite (density = 3.33 g/cm^3)			Kandelin and Weidner (1988)			*Lawsonite* (density = 3.09 g/cm^3)			Schilling et al. (2003)		
274.0	94.0	71.0	0	4.0	0	226.0	66.0	64.0	0	0	0
	253.0	82.0	0	14.0	0		216.0	83.0	0	0	0
		282.0	0	28.0	0			262.0	0	0	0
			88.0	0	13.0				64.0	0	0
				65.0	0					59.0	0
					94.0						18.0
Phengite (muscovite) (density = 2.73 g/cm^3)			Vaughan and Guggenheim (1986)			*Omphacite* (density = 3.33 g/cm^3)			Bhagat et al. (1992)		
181.0	48.8	25.6	0	−14.2	0	257.3	85.9	76.2	0	7.1	0
	178.4	21.2	0	1.1	0		216.2	71.8	0	13.3	0
		58.6	0	1.0	0			260.2	0	33.7	0
			16.5	0	−5.2				80.2	0	10.2
				19.5	0					70.6	0
					72.0						85.8
Quartz (density = 2.65 g/cm^3)			Ogi et al. (2016)			*Rutile* (density = 4.30 g/cm^3)			Isaak et al. (1998)		
86.8	6.87	11.9	−18.0	0	0	267.3	174.1	146.4	0	0	0
	86.8	11.9	18.0	0	0		0	0	0	0	0
		105.5	0	0	0			483.9	0	0	0
			58.1	0	0				123.9	0	0
				58.1	−18.0					0	0
					39.9						190.4

[a]Voigt matrix notation formulation shown in Equation 2.

the sample (Reuss, 1929), and (c) the Voigt-Reuss-Hill (VRH) average, which is the arithmetic mean of the Voigt and Reuss averages (Hill, 1952), using the method of Mainprice et al. (2011). The calculated seismic anisotropy values using the Voigt and Reuss averages were within 2% of the VRH-averaged results for all samples, therefore, we report the VRH-averaged elastic stiffness matrices throughout this work. The C^* matrix and the density of each phase (Table 2) weighted by volume fraction are used to calculate the effective elastic stiffness matrix and density of each polyphase aggregate. While recent theoretical work has proposed a first-principals-based model of elastic stiffness constants for titanite (Das et al., 2021), no single-crystal elasticity measurements are available, so this phase was excluded from the anisotropy calculations; given its low modal abundance (<7% in all blueschist samples), the exclusion of the phase in our calculations introduces some minor systematic error into these calculations.

The calculated polyphase aggregate effective elastic stiffness matrix and density were used in MTEX to solve the Christoffel (1877) equation to predict the plane wave speeds and polarizations in three dimensions; a derivation of this solution appears in the review paper by Almqvist and Mainprice (2017). The percentage of P wave seismic anisotropy (AVp) for each sample was calculated in MTEX as

$$\mathrm{AVp}\ \% = \left[\left(\mathrm{Vp}_{\max} - \mathrm{Vp}_{\min}\right)/0.5\left(\mathrm{Vp}_{\max} + \mathrm{Vp}_{\min}\right)\right] * 100 \tag{3}$$

The percentage of S wave seismic anisotropy was calculated for the fast shear waves (AVs_1) and the slow shear waves (AVs_2) as

$$\mathrm{AVs}i\ \% = \left[\left(\mathrm{Vs}i_{\max} - \mathrm{Vs}i_{\min}\right)/0.5\left(\mathrm{Vs}i_{\max} + \mathrm{Vs}i_{\min}\right)\right] * 100 \tag{4}$$

where i is 1 (fast shear wave) or 2 (slow shear wave). The shear wave splitting percentage (AVs %) for all orientations in each sample was determined as

$$\mathrm{AVs(g)}\ \% = \left[\left(\mathrm{Vs}_{1(g)} - \mathrm{Vs}_{2(g)}\right)/0.5\left(\mathrm{Vs}_{1(g)} + \mathrm{Vs}_{2(g)}\right)\right] * 100 \tag{5}$$

Where g is the orientation at which the shear wave splitting is being calculated. Maximum delay times between the fast and slow shear waves are calculated as

$$dt_{\max} = (T * AVs_{\max})/(100 * \langle Vs \rangle) \tag{6}$$

where $dt_{\max}$ is the maximum delay time, T is the thickness of the anisotropic layer, $AVs_{\max}$ is the calculated maximum shear wave splitting percentage, and $\langle Vs \rangle$ is the simple average of the shear wave phase speeds in the three principal directions (after Silver & Chan, 1991).

2.3.2. CPO Strength Measurement by Texture Index

The CPO strength of glaucophane, epidote, lawsonite, and phengite were measured using three different texture indices to test for correlation between the magnitude of seismic anisotropy and the CPO strength of these anisotropic phases. The CPO strength for each principal crystallographic axis was calculated by the pole-figure J-index (pfJ-index) as

$$\mathrm{pfJ}_{[hkl]} = \int P_{[hkl]}(\alpha,\beta)^2 d\omega \tag{7}$$

where $[hkl]$ is the Miller index of a crystallographic axis, α and β are the spherical coordinates of an orientation within the pole figure, $P_{[hkl]}(\alpha,\beta)$ is the fraction of the measured orientations of the crystallographic axis with that orientation, and $d\omega$ is the differential element (Michibayashi & Mainprice, 2004). The pfJ-index is a quantitative measure of the fabric strength of each crystallographic axis for a phase and ranges from 1 in phases with a random CPO to infinity for a single crystal orientation. The CPO strength was also calculated using the J-index, defined as

$$J = \int f(g)^2 dg \tag{8}$$

Where f(g) is the value of the ODF at orientation g, and the resulting J-index also ranges from 1 for a random CPO to infinity for a single crystal (Bunge, 1985). Fabric strength was also calculated using the misorientation angle distribution, or M-index. The misorientation angle is the minimum angle of rotation about a common axis between two grains of the same phase that are not in direct contact that will bring their respective crystal lattices into alignment (Wheeler et al., 2001). The M-index is defined as the difference between the observed misorientation angle distribution and a random distribution of misorientation angles for that phase, and is calculated as

$$M = \frac{1}{2}\int \left| R^T(\theta) - R^O(\theta) \right| d\theta \tag{9}$$

where $R^T(\theta)$ is the theoretical value of a random misorientation distribution and $R^O(\theta)$ is the observed misorientation distribution at angle θ (Skemer et al., 2005). The M-index varies from 0 for a random distribution of misorientation angles to 1 for a single crystal fabric. Functions for the calculation of these texture indices are implemented in the MTEX toolbox (Mainprice et al., 2015).

3. Results

3.1. Microstructural Description

The mineral modal analysis of the blueschists used in our seismic anisotropy calculations was conducted using the indexed areas of the EBSD maps collected on the selected representative regions of the structural reference frame-oriented thin sections. The modal abundance of the mineral phases was estimated by measuring the area fractions of each individual phase in the indexed 2-D sections of the EBSD maps. The modal abundance calculations exclude the low confidence data removed during data cleaning (Section 2.3) and the indexed titanite data (Section 2.3.1), and are used in the elastic stiffness matrix and density calculations for all samples. As discussed in Section 2.1, the mapped regions were selected to be representative of the mineralogy of the hand samples and are treated as volume fractions in the 3-D rock volumes (after Heilbronner & Barrett, 2014). Glaucophane comprises a significant fraction of all indexed phases in the EBSD maps (37%–96%), and the sample foliations and lineations are largely defined by the orientation of elongate glaucophane grains (Figures 3 and 4a–4d, 4g, 4h). Eight of the nine epidote blueschist samples contain less than 40% epidote, while sample LAB572 contains a dominant fraction of epidote (55%; Figures 4e and 4f). Elongate epidote grains are most often aligned with their longest dimension parallel to the sample foliation. The lawsonite blueschists are composed of lawsonite modes ranging from 19% to 56% occurring either as lawsonite-rich layers of anhedral grains elongated with the foliation, or subhedral porphyroblasts with no strong preferred orientations (Figures 4c and 4d). Garnet (<15%), when present, often occurs as small, anhedral grains distributed in glaucophane-rich layers, or as porphyroblasts up to 5 mm in diameter with fractures filled by glaucophane, epidote, phengite, quartz, and/or chlorite (Figures 4g and 4h). Phengite is often present in minor abundances (<2%) in these mafic-protolith blueschists (Figures 4a–4f). When present in greater abundances, phengite is associated with epidote or glaucophane, or concentrated in garnet pressure-shadows (up to ∼9%; Figures 4g and 4h). Jadeite, omphacite, quartz, chlorite, rutile, and titanite typically appear in the samples in modes <5% with limited exceptions. The error percentage of the modal abundance calculations was determined relative to the number of grains indexed for each phase as

$$\text{error \% (phase)} = \left(\frac{1}{\sqrt{N}}\right) * (\text{areal modal \%}) \tag{10}$$

where N is the number of grains indexed for the phase (Heilbronner & Barrett, 2014). The error of the modal abundances is <<1% for most phases in all samples, with a maximum error of ∼4% for the garnet fraction in LAB570 due to a significant volume of garnet (9%) contained in 5 grains (Table S1 in Supporting Information S1). The areal modal analysis of the indexed EBSD maps used in our anisotropy calculations is included in Table 3.

3.2. Crystallographic Preferred Orientations (CPOs)

Fabric development was evaluated for the minerals glaucophane, epidote, lawsonite, and phengite in each blueschist sample by calculating the pfJ-index, the J-index, and the M-index as described in Section 2.3.2. These

Table 3
EBSD-Based Areal Modal Analysis[a,b]

Sample	Gln %	Ep %	Lws %	Ph %	Grt %	Jd %	Omp %	Qz %	Chl %	Rt %
Epidote blueschist										
BAN09	60.86	38.10		0.01	0.31	0.01		0.71		
BAN15	85.78	10.35		3.80						0.07
CY106	58.89	11.29		0.78	14.48		4.64	1.32	7.68	0.93
CY107	77.87	0.28		8.57	11.93		0.12	0.51	0.69	0.04
DR221	81.60	5.59		0.28	11.91			0.08	0.13	0.41
LAB34	62.18	28.89		8.12	0.49		0.02		0.14	0.15
LAB555	95.75	0.58		0.08		0.08	0.10	3.07	0.28	0.06
LAB570	54.65	32.63		0.20	9.33			2.34	0.29	0.56
LAB572	36.94	55.39		0.91	1.77	3.27	0.06	0.29	0.05	1.32
Lawsonite blueschist										
C18G1003C01	43.02		56.26	0.03	0.28	0.31	0.05	0.01	0.04	
DR265	64.22	0.07	18.84	0.68	0.77	14.90	0.10	0.41		
GB15-02A	61.56		20.64	0.56	4.46		0.01	12.74		0.02
SV01-49A	41.61		42.94	1.51	0.85	2.69	0.08	9.89	0.21	0.22
01GSN2-3	45.74	0.03	18.70	4.04	3.13	3.17	0.12	24.83	0.04	0.21

[a]Mineral abbreviations after Whitney and Evans (2010): Gln = glaucophane, Ep = epidote, Lws = lawsonite, Ph = phengite, Grt = garnet, Jd = jadeite, Omp = omphacite, Qz = quartz, Chl = chlorite, Rt = rutile. [b]All mineral percentages are expressed as the indexed area % of each mineral from reduced EBSD data set reported by MTEX to 2 decimal places that were used in subsequent seismic anisotropy calculations (Section 3.1).

texture indices were calculated by two different procedures: (a) using the complete set of indexed EBSD orientations, and (b) as one point-per-grain (1ppg) using the mean orientation calculated from the set of all indexed orientations in each grain. The pfJ-indices (Equation 7) were determined for the [100], [010], and [001] crystallographic axes (the *a*-, *b*-, and c-axes, respectively) from pole figures calculated for each phase (complete orientation set pole figures, Figure S2 in Supporting Information S1; 1ppg pole figures, Figure S3 in Supporting Information S1). The CPO projections for the full EBSD orientation data sets are qualitatively similar to the 1ppg results, and the calculated pfJ-indices display only small deviations between the full EBSD data sets and 1ppg values. Here, we report the pfJ-index for the full sets of indexed orientations that are utilized in the seismic anisotropy calculations, but will reference the 1ppg pfJ-indices (Table S2 in Supporting Information S1) in our discussion of *P* wave seismic anisotropy and CPO strength (Section 4.2) to remain consistent with previous investigations (e.g., Cao & Jung, 2016; Fujimoto et al., 2010; Kim et al., 2013). While our analysis will focus on the correlation between the pfJ-indices of each phase and the anisotropy, we have included all pfJ-index, J-index, and M-index values for each sample calculated by both procedures in Table S2 in Supporting Information S1 for completeness.

3.2.1. Glaucophane CPOs

The glaucophane CPO in five of the samples displays the type-I amphibole CPO most prevalent in the rock record (e.g., Kim & Jung, 2019, Figures 2c and 5a), which is defined by density maxima in each of the [100], [010], and [001] principal crystallographic axes. The [001] axes display a density maximum oriented parallel to the X-direction in the specimen reference frame (the lineation direction) while the density maximum of the [100] axes is oriented normal to the foliation plane (Z-direction). The [010]-axis density maximum lies in the foliation plane, parallel to the Y-direction (defining the foliation; e.g., Figure 5a). The glaucophane in sample DR265 (Figure 5b) displays the type-III amphibole CPO (Figure 2c) that was developed in two of the samples, with an [100]-axis density maximum oriented normal to the foliation as in the type-I CPO, but is distinguished by a girdle composed of the [010] and [001] axes contained within the foliation plane. The type-IV glaucophane CPO (Figure 2c) in seven of the samples is also characterized by a [001]-axis density maximum parallel to the lineation,

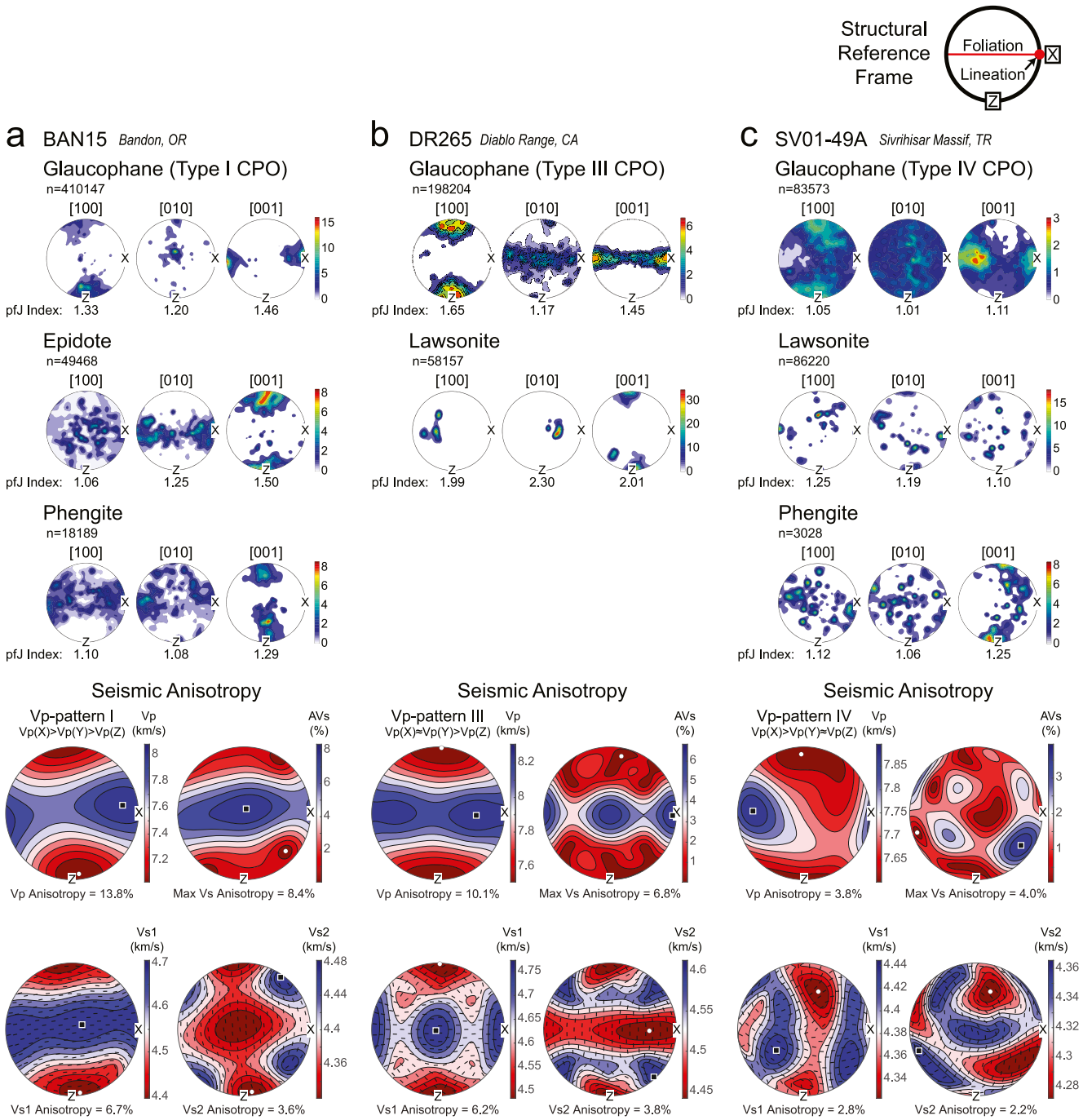

Figure 5. The CPOs in glaucophane, epidote, lawsonite, and phengite and the calculated seismic anisotropies for the full mineral assemblage for representative examples of (a) a type-I glaucophane crystallographic preferred orientation (CPO), (b) a type-III glaucophane CPO, and (c) a weak type-IV glaucophane CPO. All CPO and seismic anisotropy calculations use the full set of EBSD-indexed orientations. Pole figures are plotted as equal-area upper-hemisphere projections with multiple of uniform distribution (m.u.d.) density contours and the pole-figure J-index (pfJ-index) calculated for *n* indexed points of each phase. Phengite modal abundance is <1% in sample DR265 and is excluded from the figure. Seismic anisotropies are plotted as equal-area upper-hemisphere projections. Orientations of maximum and minimum *P* and *S* wave velocities and shear wave splitting (AVs) percentages are shown with black squares (maxima) and white circles (minima).

but differs from the type-I CPO in the [100] and [010] axes, which describe a girdle in the Y-Z plane, normal to the lineation (e.g., Figure 5c). The fabric strength of the glaucophane in the blueschist samples ranges from $pfJ_{[100]}$ = 1.05–1.65, $pfJ_{[010]}$ = 1.01–1.52, and $pfJ_{[001]}$ = 1.11–2.05 (Table S2 in Supporting Information S1).

3.2.2. Epidote CPOs

The CPO of epidote in the epidote blueschist samples most frequently occurs with a density maximum of the [010] axis oriented parallel to the lineation (Figures S2 and S3 in Supporting Information S1). Several samples with a strong epidote fabric additionally show density maxima of the [001] and [100] axes oriented normal to the sample foliation (Z-direction) and normal to the lineation within the foliation plane (Y-direction), respectively (Figures S2 and S3 in Supporting Information S1). This epidote CPO was previously described in Ile de Groix blueschists by Bezacier et al. (2010). Two of the New Caledonia epidote blueschists alternatively display a girdle of [001] and [100] axes normal to the sample lineation in the Y-Z plane (e.g., LAB570 & LAB572 in Figures S2 and S3 in Supporting Information S1). Interestingly, the observed CPOs in the nine epidote-bearing blueschists in this compilation are not reproduced in experimentally deformed blueschists (e.g., Park et al., 2020). The fabric strength of epidote in the epidote blueschists ranges from $pfJ_{[100]}$ = 1.03–2.56, $pfJ_{[010]}$ = 1.12–2.73, and $pfJ_{[001]}$ = 1.14–2.70 (Table S2 in Supporting Information S1).

3.2.3. Lawsonite CPOs

Lawsonite displays one of two fabrics depending on the distribution of the phase within the sample. In samples with large lawsonite porphyroblasts separated in a matrix of fine-grained glaucophane, the lawsonite displays a random CPO (e.g., Figure 5c). Lawsonite in samples with similar grain-size distributions as glaucophane and layers composed primarily of interconnected lawsonite grains develop a CPO with the [001]-axis density maximum oriented normal to the foliation (Z-direction) and the [100] and [010] axes oriented either as density maxima within the foliation (e.g., Figure 5b) or as a girdle parallel to the foliation plane (e.g., 01GSN2-3, Figures S2 and S3 in Supporting Information S1). Cao and Jung (2016) described this lawsonite CPO as the "normal-type" fabric, which has been frequently observed in naturally deformed lawsonite blueschists (e.g., Cao et al., 2014; Choi et al., 2021). Lawsonite fabric strength in the lawsonite blueschists covers a range of $pfJ_{[100]}$ = 1.03–1.99, $pfJ_{[010]}$ = 1.02–2.30, and $pfJ_{[001]}$ = 1.09–2.01 (Table S2 in Supporting Information S1).

3.2.4. Phengite CPOs

Phengite frequently occurs in small volumes with a weak fabric/CPO (e.g., Figure 5c). In samples with larger phengite fractions (~3%–10%), the CPO has a [001]-axis density maximum oriented normal to the foliation (Z-direction) and the [100] and [010] axes oriented in a girdle in the foliation plane (e.g., CY107, Figures S2 and S3 in Supporting Information S1). Phengite fabric strength in the blueschists ranges from $pfJ_{[100]}$ = 1.05–2.70, $pfJ_{[010]}$ = 1.06–2.70, and $pfJ_{[001]}$ = 1.24–2.78 (Table S2 in Supporting Information S1). This is typical of CPOs in micas (Lloyd et al., 2011; Mahan, 2006).

3.3. Seismic Anisotropy

The VRH-averaged effective elastic stiffness matrices in Voigt notation are shown in Table 4. The calculated Voigt matrices were used as inputs to solve the Christoffel equation (Christoffel, 1877) for the *P* and *S* plane wave velocities and polarizations, and to calculate the resultant seismic anisotropies at dry, ambient P-T conditions (AVp%, AVs_1%, AVs_2%, and AVs%; Equations 3–5). All calculated seismic properties including maximum/minimum Vp, Vs_1, and Vs_2 velocities, anisotropies, and maximum shear wave splitting orientation are included in Table 5, and stereographic projections of all calculated seismic properties are included in Figure S4 in Supporting Information S1.

The symmetry decomposition method of Browaeys and Chevrot (2004) was used to evaluate the symmetry of the Voigt elastic stiffness matrices of each sample, and the resultant anisotropy, by progressively subtracting out the isotropic, hexagonal, tetragonal, orthorhombic, and monoclinic symmetry components—leaving the triclinic component. The results of the symmetry decomposition are included in Table S3 in Supporting Information S1 as the percentage of the Voigt elastic stiffness matrix represented by the isotropic, hexagon, orthorhombic, and remaining (tetragonal, monoclinic, and triclinic) symmetry classes. The anisotropic symmetry components of the Voigt matrices were plotted on a ternary diagram to display the extent to which each sample can be represented by hexagonal, orthorhombic, or other (tetragonal + monoclinic + triclinic) symmetry (Figure S5 in Supporting Information S1). The symmetry of all the Voigt matrices is predominantly hexagonal, with LAB570 displaying the largest orthorhombic with ~2.7% orthorhombic symmetry and ~3.7% hexagonal symmetry. This dominant

Journal of Geophysical Research: Solid Earth

10.1029/2023JB027679

Table 4
VRH-Averaged Effective Elastic Stiffness Matrices in Voigt Notation[a] (in GPa)

C18G1003C01 (density = 3.08 g/cm^3)			Lawsonite blueschist (AVp = 1.5%)				*SV01-49A* (density = 3.05 g/cm^3)			Lawsonite blueschist (AVp = 3.8%)		
193.2	74.4	76.3	0.6	−0.6	0.3		187.0	64.7	66.1	0.1	−3.1	1.3
	188.1	71.6	−0.1	−0.4	−0.1			176.5	66.0	1.1	0.4	0.0
		188.8	−0.1	−0.3	0.5				181.8	0.9	−1.5	0.2
			58.3	0	−0.0					58.0	−0.2	0.1
				57.2	−0.2						58.4	0.5
					57.2							56.8
LAB572 (density = 3.31 g/cm^3)			Epidote blueschist (AVp = 6.8%)				*GB15-02A* (density = 3.05 g/cm^3)			Lawsonite blueschist (AVp = 9.0%)		
204.5	61.1	61.9	0.6	4.3	3.0		193.9	56.0	61.2	0.3	4.5	−2.2
	183.1	60.7	−0.6	0.3	1.3			165.8	54.7	0.5	0.7	−0.4
		185.5	−0.2	2.2	0.4				181.6	0.4	3.0	−0.9
			61.8	0.8	0.8					58.7	−0.1	0.5
				65.7	0.3						63.0	0.0
					64.1							59.4
CY106 (density = 3.19 g/cm^3)			Epidote blueschist (AVp = 9.5%)				*DR265* (density = 3.12 g/cm^3)			Lawsonite blueschist (AVp = 10.1%)		
219.3	61.8	65.6	1.5	2.7	1.8		211.6	59.9	75.4	−0.0	0.3	0.8
	184.7	61.7	3.0	0.1	1.1			175.8	61.3	0.2	0.2	0.4
		198.9	1.2	3.3	0.1				208.7	0.6	0.9	0.8
			64.9	0.5	0.8					62.2	0.3	−0.6
				69.5	2.0						70.9	0.3
					67.6							62.0
LAB570 (density = 3.26 g/cm^3)			Epidote blueschist (AVp = 10.2%)				*01GSN2-3* (density = 2.99 g/cm^3)			Lawsonite blueschist (AVp = 10.3%)		
215.8	58.6	63.5	0.5	−0.8	−3.4		182.8	47.9	56.1	1.8	3.0	3.0
	177.1	59.8	0.5	−0.1	−1.2			152.5	48.0	1.1	−0.1	1.3
		192.8	2.1	0.4	−0.1				175.1	2.0	1.2	1.3
			62.9	−0.4	−0.4					56.4	0.5	0.3
				68.4	1.3						61.0	0.9
					64.5							56.4
DR221 (density = 3.18 g/cm^3)			Epidote blueschist (AVp = 10.7%)				*LAB34* (density = 3.16 g/cm^3)			Epidote blueschist (AVp = 10.9%)		
218.8	60.8	63.1	1.0	−1.8	3.5		191.7	55.3	57.5	2.7	1.3	0.6
	179.7	58.6	2.3	0.1	2.0			172.6	52.9	6.8	0.1	−0.4
		193.2	2.4	−1.5	0.9				169.9	8.3	0.2	−0.4

Journal of Geophysical Research: Solid Earth

10.1029/2023JB027679

Table 4
Continued

				63.7	0.6	−0.7				58.6	−0.2	0.1
					70.3	1.1					62.0	4.0
						67.7						62.7
BAN09 (density = 3.21 g/cm^3)			Epidote blueschist (AVp = 12.8%)				*BAN15* (density = 3.10 g/cm^3)		Epidote blueschist (AVp = 13.8%)			
	205.1	54.7	*60.4*	2.0	0.4	−4.4		198.7	50.5	58.5	−1.4	2.5	−3.7
		162.1	54.7	3.3	−0.3	−2.2			154.4	51.9	−2.1	0.7	−2.0
			187.8	4.2	0.3	−0.7				189.4	−3.2	1.8	−1.1
				59.6	−1.4	−0.1					58.1	−1.3	0.3
					66.9	2.0						68.2	−0.8
						60.9							60.2
CY107 (density = 3.12 g/cm^3)			Epidote blueschist (AVp = 17.4%)				*LAB555* (density = 3.06 g/cm^3)		Epidote blueschist (AVp = 19.9%)			
	220.7	55.5	64.2	3.4	−5.1	−0.2		211.4	49.0	59.3	3.2	−1.8	6.9
		161.0	55.9	4.6	0.2	0.4			147.5	48.8	5.5	0.1	3.7
			195.7	7.4	−3.2	−0.5				188.2	7.8	−1.4	1.6
				60.4	−0.1	−0.9					58.4	1.6	0.0
					71.4	3.3						69.6	2.7
						62.1							60.5

[a]Voigt matrix notation formulation shown in Equation 2.

Journal of Geophysical Research: Solid Earth

10.1029/2023JB027679

Table 5
P and S Wave Velocities and Seismic Anisotropies at Room Temperature and Pressure

Sample	Rock type[a]	Location[b]	Vp (km/s) Max	Vp (km/s) Min	AVp (%)	Vp pattern	Gin CPO	Vs_1 (km/s) Max	Vs_1 (km/s) Min	AVs_1 (%)	Vs_2 (km/s) Max	Vs_2 (km/s) Min	AVs_2 (%)	AVs max (%)	Max shear wave splitting orientation[c]
C18G1003C01	LBS	Corsica, FR	7.92	7.81	1.5	Vp(X) > Vp (Y) ≈ Vp(Z)	Type-IV	4.36	4.31	1.0	4.34	4.30	0.9	1.3	Lineation-⊥, ∠ to foliation
SV01-49A	LBS	Sivr. Mas. TR	7.90	7.60	3.8	Vp(X) > Vp (Y) ≈ Vp(Z)	Type-IV	4.44	4.32	2.8	4.36	4.27	2.2	4.0	Lineation-‖, ∠to foliation
LAB572	EBS	Pam Penins. NC	7.93	7.40	6.8	Vp(X) > Vp (Y) ≈ Vp(Z)	Type-IV	4.51	4.39	2.8	4.42	4.30	2.7	3.8	∠ to lineation, foliation-‖
GB15-02A	LBS	Catalina CA	8.06	7.37	9.0	Vp(X) > Vp (Y) > Vp(Z)	Type-IV	4.57	4.41	3.5	4.49	4.37	2.7	4.2	∠ to lineation, foliation-‖
CY106	EBS	Tinos GR	8.32	7.56	9.5	Vp(X) > Vp (Y) > Vp(Z)	Type-IV	4.74	4.59	3.2	4.65	4.46	4.3	5.0	∠ to lineation, ∠ to foliation
DR265	LBS	Diablo Rng. CA	8.31	7.51	10.1	Vp(X) ≈ Vp (Y) > Vp(Z)	Type-III	4.77	4.49	6.2	4.61	4.44	3.8	6.8	Lineation-‖, foliation-‖
LAB570	EBS	Pam Penins. NC	8.16	7.37	10.2	Vp(X) > Vp (Y) > Vp(Z)	Type-IV	4.67	4.43	5.2	4.53	4.35	4.2	6.2	∠ to lineation, foliation-‖
01GSN2-3	LBS	S. Motagua GT	7.90	7.13	10.3	Vp(X) > Vp (Y) > Vp(Z)	Type-I	4.56	4.34	5.0	4.44	4.33	2.9	5.3	∠ to lineation, foliation-‖
DR221	EBS	Diablo Rng. CA	8.32	7.48	10.7	Vp(X) > Vp (Y) > Vp(Z)	Type-IV	4.75	4.60	3.2	4.63	4.47	3.7	5.6	Lineation-⊥, foliation-‖
LAB34	EBS	Diablo Rng. CA	7.82	7.01	10.9	Vp(X) ≈ Vp (Y) > Vp(Z)	Type-III	4.60	4.32	6.4	4.34	4.27	1.7	6.7	Lineation-‖, foliation-‖
BAN09	EBS	Bandon OR	8.01	7.05	12.8	Vp(X) > Vp (Y) > Vp(Z)	Type-I	4.61	4.32	6.5	4.44	4.29	3.5	7.0	Lineation-⊥, foliation-‖
BAN15	EBS	Bandon OR	8.08	7.04	13.8	Vp(X) > Vp (Y) > Vp(Z)	Type-I	4.70	4.40	6.7	4.48	4.32	3.6	8.4	Lineation-⊥, foliation-‖
CY107	EBS	Tinos GR	8.47	7.12	17.4	Vp(X) > Vp (Y) > Vp(Z)	Type-I	4.84	4.43	8.8	4.60	4.35	5.7	10.0	Lineation-⊥, foliation-‖
LAB555	EBS	Pam Penins. NC	8.36	6.84	19.9	Vp(X) > Vp (Y) > Vp(Z)	Type-I	4.82	4.40	9.2	4.53	4.33	4.4	10.4	Lineation-⊥, foliation-‖

[a]Rock Type: LBS = lawsonite blueschist, EBS = epidote blueschist. [b]Sample peak P-T condition estimates from the literature included in Table 1. [c]Max shear-splitting orientation notations: ⊥ = normal, ‖ = parallel, ∠ = at an angle (~30–60°).

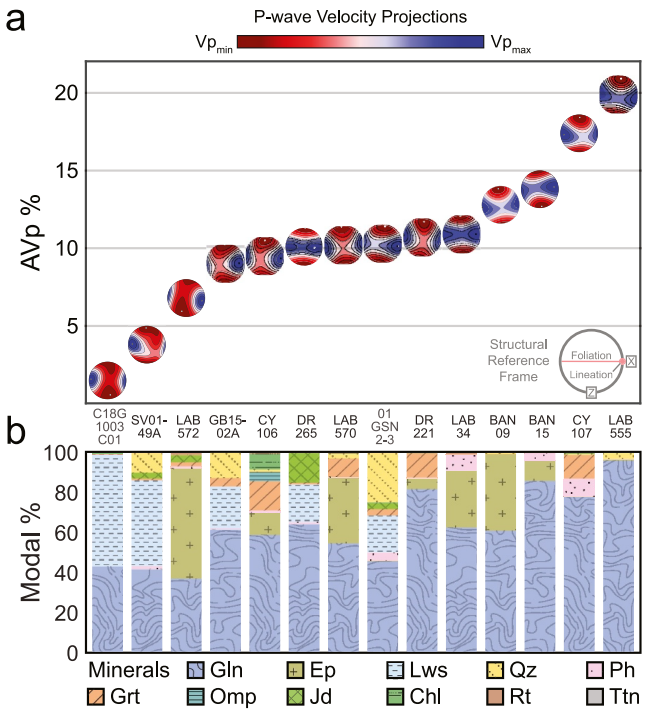

Figure 6. (a) The calculated upper-hemisphere *P* wave velocity projections plotted in order of increasing maximum Vp anisotropy (AVp %) displays the broad range of seismic anisotropy presented in the compilation samples. The *P* wave anisotropy patterns are positively correlated with the crystallographic preferred orientation type observed in glaucophane for each sample. (b) The modal composition of each sample follows a general trend of increasing AVp with increasing glaucophane modal abundance.

contribution of hexagonal symmetry to anisotropy in blueschists is consistent with the results of Brownlee et al. (2017) for amphibole-rich deep crustal rocks.

3.3.1. *P* Wave Seismic Anisotropy

The maximum *P* wave velocities of all blueschists in the compilation are oriented within the sample foliation and parallel to sub-parallel to the lineation and range from Vp_{max} = 7.82 km s^{-1} (LAB34) to 8.47 km s^{-1} (CY107). The minimum *P* wave velocities of the samples are oriented normal to the foliation plane and range from Vp_{min} = 6.84 km s^{-1} (LAB555) to 7.81 km s^{-1} (C18G1003C01). Figure 6a displays the patterns of the *P* wave velocities for each sample plotted as contoured, equal-area, upper-hemisphere spherical projections in order of increasing AVp. The blueschists in this study display a broad range of *P* wave anisotropies extending from a minimum AVp = 1.5% for the lawsonite blueschist C18G1003C01 from Corsica, France to a maximum AVp = 19.9% for the epidote blueschist LAB555 from the Pam Peninsula, New Caledonia (Table 5). The salient feature of the *P* waves anisotropies in Figure 6a is that half of the blueschist samples show AVp values ~10%, despite their variance in mineral assemblages (Figure 6b).

The upper-hemisphere spherical projections of the *P* wave velocities display three different seismic anisotropy patterns that were previously observed in amphibolite facies deep crustal rocks (Ji et al., 2013; Kim & Jung, 2020; Liu & Cao, 2023). We describe the patterns using the terminology of Liu and Cao (2023) where Vp(X) is the velocity in the X-direction (parallel to the lineation), Vp(Y) is the velocity in the Y-direction (normal to the lineation in the foliation plane), and Vp(Z) is the velocity in the Z-direction (normal to the foliation plane). In the blueschists with the highest AVp % magnitudes, the Vp pattern is Vp(X) > Vp(Y) > Vp(Z) and is correlated to a type-I CPO in glaucophane (Figure 5a). The two blueschists in our study with a type-III CPO in glaucophane display Vp patterns with Vp(X) ≈ Vp(Y) > Vp(Z) (Figure 5b). Blueschists with the lowest AVp % magnitudes display Vp patterns with Vp(X) > Vp(Y) ≈ Vp(Z) and glaucophane with a type-IV CPO (Figure 5c). In the remainder of the text, these Vp patterns will be referred to as Vp-pattern I (Vp(X) > Vp(Y) > Vp(Z)), Vp-pattern III (Vp(X) ≈ Vp(Y) > Vp(Z)), and Vp-pattern IV (Vp(X) > Vp(Y) ≈ Vp(Z)) based on their association with the observed CPO types of the same number.

3.3.2. *S* Wave Seismic Anisotropy

The fast and slow shear wave maximum/minimum velocities are included in Table 5, and result in calculated seismic anisotropies ranging from AVs_1 = 1% and AVs_2 = 0.9% (C18G1003C01) to AVs_1 = 9.2% and AVs_2 = 5.7% (LAB555). The calculated AVs_1, AVs_2, and AVs percentages do not follow the same trend of increasing magnitude that is observed in the blueschist AVp percentages (Figure S6 in Supporting Information S1), and two of the samples yield AVs_2 percentages that are larger than AVs_1 (e.g., Figure S6 in Supporting Information S1, CY106 and DR221). For all samples other than C18G1003C01, the fast shear wave polarization is contained within the foliation for S_1 waves propagating along the X-Y plane and parallel to the lineation for S_1 waves propagating in the Z-direction (Figure 5 and S4 in Supporting Information S1). In the lawsonite blueschist C18G1003C01, the polarizations of the fast shear waves are reversed from that observed in the other blueschists of the compilation (Figure S4 in Supporting Information S1).

The Corsican lawsonite blueschist, C18G1003C01, displays the lowest magnitude of maximum shear wave splitting (AVs_{max} = 1.3%) and the epidote blueschist LAB555 from New Caledonia displays the highest magnitude of shear wave splitting (AVs_{max} = 10.4%). The maximum shear wave splitting percentage of most samples is less than 7% and most often is contained within the foliation plane with orientations varying from lineation-parallel to lineation normal (Table 5, Figure S4 in Supporting Information S1). The calculated AVs magnitudes generate modest Vs_1/Vs_2 delay times in blueschist layers with thicknesses observed in exhumed

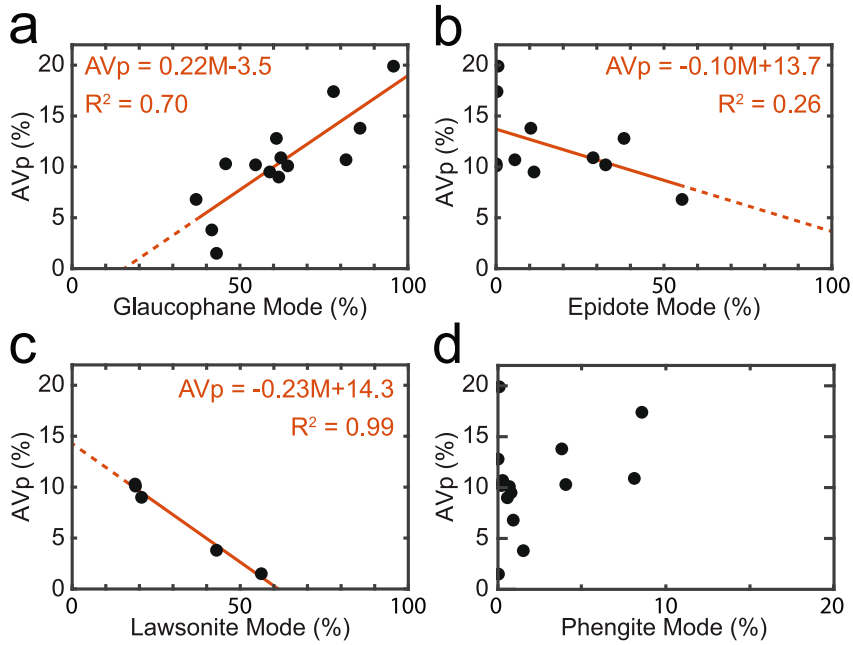

Figure 7. AVp % versus mineral mode (%) of samples for (a) glaucophane, (b) epidote, (c) lawsonite, and (d) phengite. AVp trends for glaucophane, epidote, and lawsonite are fit by linear regression and the equations of the best-fit line (with M = modal abundance of the phase), and the R^2 quality of fit statistic shown.

subduction terranes or with thicknesses of the same order as oceanic crust (~7 km) except for steep subduction angles (~45–60°; e.g., Cao et al., 2013; Ha et al., 2019; Park & Jung, 2022).

4. Discussion

Below, we explore the effect of variations in modal mineralogy and CPO strength on the seismic anisotropy of mafic blueschists. *S* wave anisotropy, and the resultant shear wave splitting delay times between Vs_1 and Vs_2, are tools that are useful to understanding the seismic anisotropy of the mantle wedge (Long, 2013). However, the technique is a path-integrated measurement that provides weak constraints on the depth of the anisotropic layer; application of the technique is further complicated by the small delay times our AVs results generate in blueschist units with thicknesses observed in exhumed blueschist units (10s to a few 1000s of m). In contrast, receiver function analysis of *P* to *S* conversions of teleseismic waves can resolve contrasts in anisotropy to ~2 km in thickness (Schulte-Pelkum & Mahan, 2014b), and shows potential for imaging blueschist-metamorphosed oceanic crust (Long, 2013), therefore, we focus on AVp, while reporting calculated shear wave splitting values in Figure S4 in Supporting Information S1. We first consider the effect of modal composition and CPO strength independently on the resulting AVp. Next, we consider the combined effects of mineralogy and CPO strength by modeling two-phase aggregates, and the impact of increasing metamorphic grade on the *P* wave anisotropy. Lastly, we explore the implications of blueschist anisotropy for the investigation of subduction zones.

4.1. AVp % and Modal Composition

While the blueschists of our study display a wide range of *P* wave anisotropy (1.5%–19.9%; Figure 6a; Table 5), we note that the samples are composed primarily (>70%) of the minerals glaucophane, epidote, lawsonite, and phengite—each of which is strongly anisotropic (Figure 6b). We plotted the AVp as a function of the modal composition of each phase and found a clear positive correlation between the abundance of glaucophane and the resultant AVp of the sample (Figure 7a). Increasing fractions of either epidote (Figure 7b) or lawsonite (Figure 7c) correspond to a reduction of the sample AVp. Although phengite is the most anisotropic phase commonly found in blueschists, we observed no trend between increasing modal abundance of phengite and the AVp magnitude of the samples (Figure 7d). This lack of clear correlation between increasing fractions of phengite and AVp magnitude is likely due to weak phengite fabrics and a relatively low phengite abundance (typical of mafic

blueschists). The four samples containing phengite fractions greater than 3% display *P* wave anisotropy magnitudes >10% (Table 5), signifying a potential contribution by phengite to the magnitude and symmetry of the anisotropy if it occurs in higher abundances. The increase in AVp with increasing glaucophane modal abundance and decreasing AVp with increasing epidote or lawsonite are consistent with the measured single-crystal seismic properties of each phase (Figure 2b; Bezacier et al., 2010; Aleksandrov et al., 1974; Schilling et al., 2003), where glaucophane is the most anisotropic mineral of the three with respect to *P* waves.

To evaluate the extent to which each mineral phase enhances or dilutes the bulk seismic anisotropy, we modeled the relationship between the AVp and mineral mode by linear regression for glaucophane, epidote, and lawsonite (Figures 7a–7c). Multivariate linear regression would be a tool to model the trend in AVp as a contribution from multiple uncorrelated variables, however, the modal fractions of an aggregate do not vary independently, thus precluding this approach. Consequently, we modeled the relationship between each phase and the bulk AVp by single linear regression. Best-fit lines to the anisotropy trends in glaucophane and epidote display slopes of +0.22 for the AVp % versus glaucophane abundance and −0.10 for the AVp % versus epidote abundance, respectively (Figures 7a and 7b), a relationship that reflects the contrast in single-crystal *P* wave anisotropy between glaucophane (max AVp = 38.1%) and epidote (max AVp = 26.5%). The single-crystal anisotropy of lawsonite (max AVp = 24.1%) is similar to that of epidote, and so a similar trend might be expected. However, the best-fit line for AVp versus lawsonite abundance shows a slope of −0.23 (Figure 7c). The dilution of the bulk anisotropy cannot be explained solely by the difference in mode between glaucophane and lawsonite, or by glaucophane mode alone; some samples with similar modes have large variations in anisotropy. Thus, we must include the effect of CPO on the seismic anisotropy generated by each phase, a relationship we explore below.

4.2. AVp % and CPO Strength

Previous work on the seismic anisotropy of deformed rocks links the development of significant seismic anisotropy to the creation of strong CPOs by plastic deformation processes (e.g., Almqvist & Mainprice, 2017; Mainprice & Nicolas, 1989). We observe a strong correlation between the glaucophane CPO type (Figures 2c and 5 and S2, S3 in Supporting Information S1), the AVp magnitude, and the symmetry of the AVp patterns (Figure 6a; Table 5). Blueschists with a type-I glaucophane CPO display Vp-pattern I, and result in AVp percentages from 10.3% to 19.9%. The two blueschists with type-III glaucophane CPOs display Vp-pattern III, and yield AVp percentages of 10.1% and 10.9%. Blueschists with type-IV glaucophane-CPOs transition from Vp-pattern IV in samples with the lowest *P* wave anisotropy (AVp = 1.5%–6.8%) to Vp-pattern I with higher *P* wave anisotropies (AVp = 9%–10.7%). This transition in the Vp pattern is accompanied by increased density of the [100] and [010] crystallographic axes in the Z- and Y-directions respectively that implies a transition between the type-IV and type-I amphibole CPOs in these samples. The magnitude of AVp percentages of the blueschists in our compilation can be broadly ordered as AVp(Vp-pattern I) > AVp(Vp-pattern III) > AVp(Vp-pattern IV) in agreement with the trend observed for the hornblende-group amphiboles in amphibolites (Figure 8a; Ji et al., 2013; Kim & Jung, 2020; Liu & Cao, 2023). We infer from these results that the glaucophane CPO strength and type exerts a strong control on the magnitude and symmetry of the *P* wave seismic anisotropy in blueschists.

To explore the effects of CPO strength of each crystallographic axis on the magnitude of the *P* wave seismic anisotropy, we plotted the AVp versus the pfJ-index (calculated as 1ppg) for the [100], [010], and [001] crystallographic axes for glaucophane, epidote, lawsonite, and phengite. We colored each datapoint by Vp pattern and modeled the AVp versus pfJ-index trends using linear regression to assess the dependence of the seismic anisotropy magnitude on the CPO strength of each phase (Figure 8). After performing a Pearson correlation test (Freedman et al., 2007), we determined the strength of correlation between the pfJ-indices and AVp magnitude and the confidence interval of the fit did not justify a multivariate linear regression, therefore, we used single linear regression for this analysis. We excluded two outliers (DR265 and 01GSN2-3; Figure 8a, open circles) from the best-fit results for glaucophane. We observed steep increases in AVp with the pfJ-index of the glaucophane axes, with a positive correlation in the [100] axis (slope = 33.84, R^2 = 0.77), and a weak AVp to pfJ-index relationship for the [010] axis (slope = 44.07, R^2 = 0.41) and [001] axis (slope = 13.47, R^2 = 0.33; Figure 8a). In epidote and lawsonite, the increase in pfJ-index of each crystallographic axis weakly correlates with shallow increases in AVp (slopes <10; Figures 8b and 8c), and phengite does not display a clear linear relationship between CPO strength and sample AVp (Figure 8d).

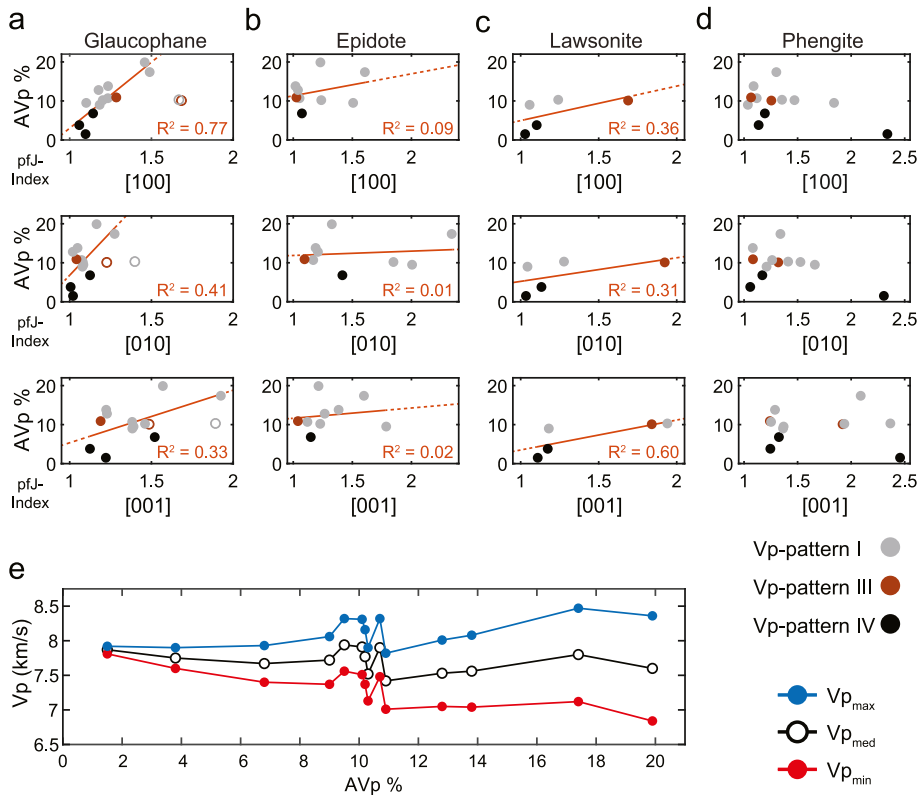

Figure 8. AVp % vs. the pfJ-Index for the [100] axis, [010] axis, and [001] axis for (a) glaucophane, (b) epidote, (c) lawsonite, and (d) phengite. Best-fit linear regression AVp/pfJ-index trendlines are shown with R^2 quality of fit statistic shown for glaucophane, epidote, and lawsonite. $R^2 = 1$ if 100% of data explained by fit, and decreases to 0 for lower fit-quality. Markers are colored by Vp pattern (see text) and open markers (a) are excluded from the linear regression fit (see text); (e) $Vp_{maximum}$, Vp_{median}, and $Vp_{minimum}$ versus AVp % for all blueschists in this study.

The qualitative relationship between glaucophane CPO type, the Vp pattern symmetry, and AVp magnitude implies that strong alignment of the glaucophane [100] and [010] axes enhances blueschist anisotropy. It is notable that we do find a moderately strong CPO in the [001] axis in all of our samples, even when the [100] and [010] axes are weakly oriented. Alignment of the [001] axis generates low-magnitude seismic anisotropy which is typical in the early stages of ductile deformation of blueschists (Park et al., 2020). The strong increase in AVp with CPO strength in the glaucophane [100] and [010] axes (Figure 8a) suggests that strong alignment of these axes exerts a key control on the resultant anisotropy magnitude (and Vp pattern). To evaluate the relative importance of the glaucophane [100] and [010] axes to the bulk anisotropy, we plotted each sample's calculated maximum, minimum, and median *P* wave velocities versus the AVp percentage in Figure 8e. Vp_{max} increased by ~5.5% (from 7.92 km s^{-1} to 8.36 km s^{-1}) between the least anisotropic sample (C18G1003C01, AVp = 1.5%) and most anisotropic sample (LAB555, AVp = 19.9%). We observed decreases in Vp_{min} and the median *P* wave velocity (Vp_{med}) of ~12.4% (from 7.81 km s^{-1} to 6.84 km s^{-1}) and ~3.4% (from 7.87 to 7.6 km s^{-1}), respectively, between the two samples. We associate the reduction in Vp_{min}—the greatest change in Vp in our results—with stronger alignment of the glaucophane [100] axis after the single-crystal elasticity measurements of Bezacier et al. (2010). Based on this analysis, we assert that the strength of the CPO in the [100] axis exerts the strongest control on the magnitude and symmetry of seismic anisotropy in mafic blueschists, once the [001] axis is already aligned.

4.3. AVp % of Two-Phase Rock Recipe Models

Based on the restrictions that exclude the application of multivariate regression analysis of our data, we applied an alternative approach of rock recipe modeling to explore the relative contributions of mineral abundances and CPO

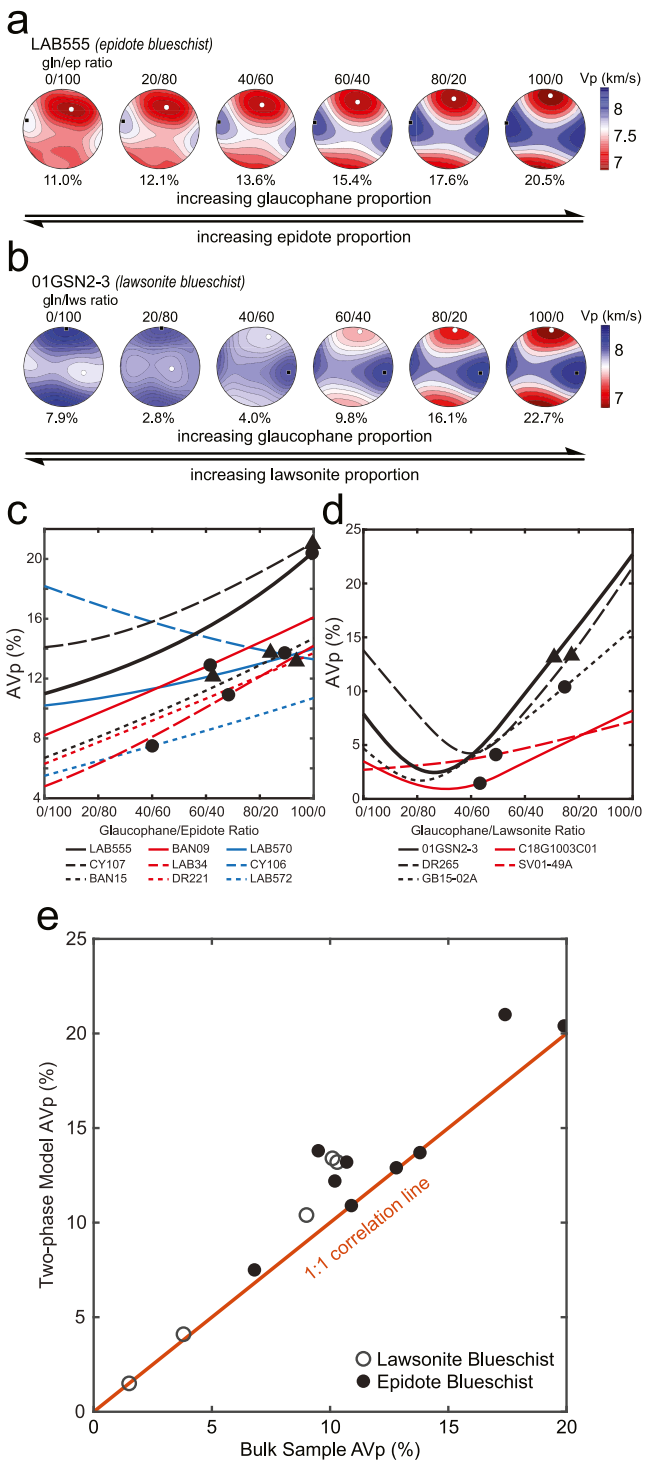

Figure 9.

strength to the bulk seismic anisotropy of our compilation samples (e.g., Bernard et al., 2021; Lloyd et al., 2011; Ward et al., 2012). We constructed two-phase rock recipe models for each sample using the ODFs that were calculated for glaucophane and epidote or lawsonite in the full mineral assemblage. We then modeled the Vp anisotropy patterns and AVp percentage by the same method as for the full mineral assemblages, but limited to normalized ratios of glaucophane/epidote (Gln/Ep; epidote blueschists) or glaucophane/lawsonite (Gln/Lws; lawsonite blueschists) ranging from 0 to 100% glaucophane (Figure 9 and S7 in Supporting Information S1). Our methodology assumes that the CPO strength of each phase in the naturally deformed polyphase rocks will remain constant across the range of compositions in the modeled two-phase aggregates. In situ, strain-partitioning in a naturally deformed rock depends on the total magnitude of strain and strain-rate experienced by the rock, the temperature under which the rock was deformed, and strength contrasts between adjacent phases (Lloyd et al., 2011; Park et al., 2020). These limitations should be considered when extending these modeling results to natural samples.

4.3.1. Epidote Blueschist AVp Modeling

The Vp anisotropy pattern modeling results for a representative epidote blueschist sample (LAB555) are displayed in Figure 9a for the glaucophane/epidote ratios: 0/100, 20/80, 40/60, 60/40, 80/20, and 100/0. The glaucophane and epidote in this sample have moderately strong, complementary CPOs (Figures S2 and S3 in Supporting Information S1; Table S2 in Supporting Information S1), consequently, the AVp is substantial for all modeled Gln/Ep ratios and monotonically increases from 11.0% to 20.5% with increasing glaucophane fraction (Figures 9a–9c). Vp_{max} and Vp_{min} remain oriented parallel to the lineation and normal to the foliation respectively for all modeled Gln/Ep ratios.

Our rock recipe models of the remaining epidote blueschists in this compilation similarly show monotonic increases in AVp on the order of ~5%–10% between the pure epidote and pure glaucophane models (Figure 9c) with the exception of CY106. This sample is composed of strongly aligned epidote and glaucophane with a weak type-IV CPO (Figures S2 and S3 in Supporting Information S1), and exhibits a decrease in AVp with increasing glaucophane. While CY106 contains ~8% chlorite with a preferred orientation (Figures S2 and S3 in Supporting Information S1), a phase that also may contribute substantially to seismic anisotropy (Kang & Jung, 2019; Kim et al., 2020;

Figure 9. Equal-area upper hemisphere stereographic projections of *P* wave velocities (in km/s) and AVp % for (a) the range of Gln/Ep ratios for epidote blueschist LAB555 and (b) the range of Gln/Lws ratios for lawsonite blueschist 01GSN2-3. Projections show increasing glaucophane proportion from left-to-right and maximum and minimum *P* wave velocity orientation with black and white markers, respectively; (c) AVp trends with increasing glaucophane in 2-phase models for all epidote blueschists in the study and (d) AVp trends with increasing glaucophane in 2-phase models for all lawsonite blueschists. Markers on each profile in part c and d correspond to Gln/Ep or Gln/Lws ratio in bulk sample and are represented as circles for models matching bulk AVp within 2%, and triangles for modeled AVp higher (up to ~5%) than bulk sample AVp %. (e) Scatterplot of the calculated AVp % for bulk sample versus the calculated AVp % of the 2-phase models at the Gln/Ep or Gln/Lws ratios in the bulk sample. The 1:1 correlation line illustrates where samples would plot if the calculated AVp % coincides for both methods.

Kim & Jung, 2015), the AVp prediction of our two-phase model is ∼5% higher in magnitude than for the bulk assemblage calculation (Figure 9c; Table 5). Though CPOs of glaucophane and epidote are not fully complementary in all samples (e.g., Figures S2 and S3 in Supporting Information S1, LAB34 and LAB572), we found the orientation of the maximum and minimum *P*-wave velocities reflected the glaucophane CPO in all models with 20% or greater fractions of glaucophane (Figure S7 in Supporting Information S1), meaning it controls the anisotropy orientation. The 100% glaucophane models in Figure 9c display ∼10% difference in AVp magnitude between a sample with a weak type-IV glaucophane CPO (LAB572) and a strong type-I glaucophane CPO (CY107). Taken together with our discussion of AVp dependence on modal abundance and CPO for the full sample mineral assemblages, these models imply that the seismic anisotropy of epidote blueschists is largely controlled by the modal abundance and CPO of glaucophane.

4.3.2. Lawsonite Blueschist AVp Modeling

Vp anisotropy pattern models for sample 01GSN2-3, a lawsonite blueschist with strong type-I glaucophane CPO and normal-type lawsonite CPO, are presented in Figure 9b across a range of glaucophane/lawsonite ratios. The antithetically aligned fast-velocity axes of glaucophane and lawsonite in the sample (Figures 2b, S2, S3 in Supporting Information S1; Table S2 in Supporting Information S1) result in a concave AVp profile with maximums of 7.9% and 22.7% for models with Gln/Lws ratios of 0/100 and 100/0, respectively (Figures 9b–9d). The minimum AVp ∼2.5% occurs at a modeled composition of ∼25% glaucophane; below this threshold, the orientation of the *P* wave velocities are controlled by the lawsonite CPO with Vp_{max} oriented normal to the foliation and Vp_{min} contained within the foliation plane (Figures 2b and 9d). With >25% glaucophane, the velocity structure reflects the glaucophane CPO, with Vp_{max} parallel to the lineation and Vp_{min} normal to the foliation (Figures 2b and 9d).

The concave AVp profile of the 01GSN2-3 models was observed previously in lawsonite blueschists (e.g., Kim et al., 2013), and we found similar profiles in the rock recipe modeling for four of the five lawsonite blueschists included in this work (Figure 9d). The minimum AVp of these models ranged from ∼1% to 4.2% and occurred at glaucophane fractions of 20%–40%. We note that the glaucophane/lawsonite ratio of the AVp minimum, and the accompanying shift of the anisotropy orientation from lawsonite CPO to the glaucophane CPO, does not trend with the pfJ-indices of either phase (Table S2 in Supporting Information S1), but depends on the combined CPO strengths of both phases. The AVp profile of sample SV01-49a differs from the other lawsonite blueschists in our compilation. This sample from the Sivrihisar Massif contains larger (>200 μm), unaligned lawsonite porphyroblasts in a matrix of glaucophane with a weak type-IV CPO (Figure 5c). With no contradictory CPO in lawsonite, our models display a weakly increasing AVp with larger fractions of glaucophane (Figure 9d) peaking at an AVp of 7.2%, and an anisotropy profile similar to our models for epidote blueschists (Figure 9c). In this case, unaligned lawsonite acts to dilute the seismic anisotropy, inversely proportional to glaucophane mode.

These results demonstrate that the effect of lawsonite on blueschist seismic anisotropy can be considerable. The contradictory alignment of Vp_{max} and Vp_{min} in strongly aligned lawsonite versus glaucophane rapidly diminishes the contribution of glaucophane to the anisotropy and produces the steeply negative slope in AVp for our samples with increasing lawsonite abundance relative to epidote (Figures 7b and 7c). Dilution of the anisotropy by strongly aligned lawsonite has been invoked previously to explain generally lower magnitude of seismic anisotropy observed in lawsonite blueschists (Cao & Jung, 2016; Kim et al., 2013). However, our models demonstrate that lawsonite blueschists with dominant fractions of glaucophane (>80%) may generate AVp anisotropies indistinguishable from epidote blueschists. The dependence of AVp magnitude on glaucophane CPO strength is further supported in our 100% glaucophane models; we observed a broader range of AVp magnitudes (∼15%) than found in our epidote blueschist two-phase models (Figure 9d).

4.3.3. Modeled AVp Versus Bulk Sample AVp

Comparison of the AVp of our two-phase models with the AVp of the bulk sample composition illustrates that the presence of significant fractions of phases with lower elastic anisotropies or weak CPOs may dilute the anisotropy of blueschists. For each modeled AVp profile, we plotted the Gln/Ep (Figure 9c) or Gln/Lws (Figure 9d) ratio of the respective sample. Figure 9e is a comparison plot of the AVp of the two-phase model versus the bulk sample calculations for all samples. The AVp percentage of the two-phase models and bulk sample calculations matched within 2% for 8 of 14 blueschists (Figures 9c and 9d, circles). The AVp of the remaining 6 models were 2%–5%

higher than bulk sample calculations (Figures 9c and 9d, triangles). Two-phase models with high AVp compared to the bulk sample calculations correlated to samples containing significant fractions of garnet (up to ∼15%; CY106, CY107, DR221, DR265, 01GSN2-3), phengite (up to ∼9%; CY107, 01GSN2-3), jadeite (∼15%; DR265), chlorite (∼8%; CY106), or quartz (up to ∼24%; LAB570, 01GSN2-3). While the dilution of the anisotropy may be attributed to the high abundance and low elastic anisotropy of garnet in some cases (e.g., CY106, CY107, DR221), in DR265 the lower AVp of the bulk sample calculation stems from the CPO and lower elastic anisotropy of jadeite (Table 3, Figures S2 and S3 in Supporting Information S1). The differences between our two-phase models and the bulk samples shows we should regard such two-phase models as a maximum bound on the anisotropy generated by blueschists. However, it is notable that the two-phase models produce similar AVp % predictions as the full mineral assemblages in most models, highlighting the key role played by the glaucophane, lawsonite, and epidote in generating seismic anisotropy in mafic blueschists (Figure 9e).

4.4. Seismic Anisotropy and Increasing Metamorphic Grade

Lawsonite is stable in the lowest grade and coldest temperatures to high pressure conditions of blueschist-facies rocks (lawsonite blueschist facies), while epidote is stable in the warmer, moderate pressure epidote blueschist-facies rocks (Evans, 1990). Therefore, we examined our data for trends in the magnitude of the anisotropy in AVp, AVs_1, AVs_2, and AVs as a function of pressure, temperature, and temperature/pressure (Figure S8 in Supporting Information S1). The epidote blueschists display generally higher *P* and *S* wave anisotropies than lawsonite blueschists, in agreement with the observations of other workers (e.g., Bezacier et al., 2010; Cao et al., 2013; Fujimoto et al., 2010; Kim et al., 2013; Park et al., 2020), but we observe no clear trends between the peak P-T conditions experienced by our samples and the magnitude of the seismic anisotropy.

The relationship between seismic anisotropy and increasing metamorphic grade is further complicated by the poorly constrained effects of pressure and temperature on each phase and the full mineral assemblages of each sample. The elastic stiffness constants for many of the constituent phases in blueschist have been measured at only ambient conditions, with few experimental studies to evaluate the sensitivity of the elastic constants to high pressures (e.g., garnet by Chai et al., 1997) or temperatures (e.g., rutile by Isaak et al., 1998). Therefore, our anisotropy calculations were conducted at dry, ambient conditions. An experimental study on an epidote blueschist and two lawsonite blueschists shows decreasing AVp until pressures ∼0.7 GPa (attributed to the closing of microcracks in the samples), a weakly decreasing AVp at pressures of 0.7–1 GPa at a constant temperature of 20°C, and weakly increasing AVp at temperatures of 20–400°C at a constant confining pressure of 1 GPa (Fujimoto et al., 2010). In contrast, a density functional theory based study of glaucophane's elasticity at high pressures reports a significant reduction in AVp from ∼36% at ambient pressure to ∼27% at 4 GPa (Mookherjee & Bezacier, 2012). Combined with the key role glaucophane plays in our AVp models, this suggests pressure effects on the magnitude of seismic anisotropy may be important well beyond the depth of microcrack closure.

Because of the contrary alignment of the fast and slow velocity directions in typical glaucophane and lawsonite CPOs, replacement of lawsonite by epidote with increasing temperatures might enhance the seismic anisotropy. Such enhancement of the anisotropy is dependent on growth of epidote in the complementary CPO to glaucophane frequently observed in epidote blueschists. There are examples in the rock record of epidote pseudomorphs after lawsonite (e.g., Hamelin et al., 2018), but we found no examples of studies that considered the CPOs of lawsonite and epidote in such replacement reactions. If we treat the range of epidote, lawsonite, and glaucophane CPOs in this study as representative and consider an example with a significant lawsonite composition of 40% with the simplifying assumption that all lawsonite is replaced by epidote, then our two-phase rock recipe models yield AVp ranges of 3%–10% for lawsonite blueschists and higher anisotropies of 8%–17% for epidote blueschists (Figures 9c and 9d). This dilution of the anisotropy due to the lawsonite CPO in our models diminishes with decreasing lawsonite abundance.

A more complete understanding of the seismic anisotropy of blueschists with increasing metamorphic grade will require ongoing collaborative work between the geology and rock and mineral physics communities, including elasticity measurements of the constituent phases of blueschists to high pressures and temperatures to facilitate extrapolation of petrofabric-based anisotropy calculations to P-T conditions at the subduction interface in active subduction zones. Texture-related seismic anisotropy studies of samples from exhumed subduction terranes spanning the lawsonite-epidote blueschist transition are needed to assess if these models are representative of the

evolution of the anisotropy during the transition. Finally, this work needs to be validated by additional in situ measurements of anisotropy in mafic blueschists with varying mineralogies and fabric strengths under dry and wet conditions to account for the effects of pressure, temperature, and fluid pressure on seismic anisotropy.

4.5. Implications for Seismic Anisotropy of Subduction Zones

P wave seismic tomography models of subducting crust under Java (Koulakov et al., 2009), Japan (Wang & Zhao, 2008, 2012, 2021), and Alaska (Tian & Zhao, 2012) yield azimuthal anisotropies ranging from ~3 to 10%. While our calculated *P* wave anisotropies do extend to greater magnitudes than the tomographic models, it has been noted that the actual magnitude of the seismic anisotropy may be reduced by the damping and smoothing routines applied in tomographic inversions (e.g., Wang & Zhao, 2021). The blueschists in our compilation typically display higher AVp values than eclogites (<6%; e.g., Bezacier et al., 2010; Cao & Jung, 2016; Mauler et al., 2000; Worthington et al., 2013), and while the range of AVp overlaps with peridotites (up to ~15%), the *P* wave velocity of blueschists are typically lower (blueschist Vp_{min}–Vp_{max} = 6.8–8.5 km/s; peridotite Vp_{min}–Vp_{max} = 7.6–8.9 km/s; e.g., Worthington et al., 2013; Liu et al., 2019; Bernard et al., 2021). The *P* wave velocities and anisotropies in this work are useful as natural constraints to differentiate blueschist from other anisotropic lithological units in subduction zones.

The plateau observed at AVp ~10% in seven of our samples merits additional consideration as this represents a potential constraint on the *P* wave anisotropy of blueschist in active subduction zones. While EBSD-based petrofabric studies of seismic anisotropy report AVp values up to 30%, AVp values ~10% are frequently calculated for blueschists in the literature (Cao et al., 2014; Cao & Jung, 2016; Kim et al., 2013; Park & Jung, 2022). Our EBSD-based results predict the *P* wave anisotropy using rock textures measured at mm scales under ambient conditions, but are consistent with AVp values determined by petrophysical methods using larger sample volumes in the literature. Keppler et al. (2017) measured the CPOs of two mafic blueschists using neutron diffraction and calculated AVp values ~ 6.5% and 12%. Fujimoto et al. (2010) and Zertani et al. (2022) measured AVp values ~11% using ultrasonic pulse transmission at elevated P-T conditions (up to 400°C at 1 GPa and 600° C at 600 MPa, respectively). Application of these constraints to interpretation of geophysical data requires consideration of macroscopic geological structure and rock heterogeneities, which can reduce the magnitude and change the symmetry of the observed anisotropy (Okaya et al., 2018; Zertani et al., 2020). Further work integrating micro to outcrop scale observations with macroscale structural features of exhumed, coherent subduction terranes is needed to assess the effects of meso-scale structures on this reported suite of microstructural-based constraints.

Shear wave splitting delay times have been reported in subduction zones ranging from 0.3 s in the Nicaragua subduction zone up to 4.5 s in the Hikurangi subduction zone (e.g., Abt et al., 2009; Currie et al., 2004; Greve et al., 2008; Long & van der Hilst, 2006). The orientation of the fast shear wave, Vs_1, is most frequently observed parallel to the trench (Long, 2013), but trench-normal Vs_1 orientations have been observed in a limited number of subduction zones including the Cascadia subduction zone (Currie et al., 2004) and the Nicaragua subduction zone (Abt et al., 2009). Taking the lineation direction as indicative of the direction of subduction with a 5-km thick anisotropic layer, the New Caledonian blueschist LAB555 can generate trench-parallel anisotropy with a delay time of dt_{max} ~ 0.1s (Equation 6). The Diablo Range blueschist, LAB34, can generate trench-normal anisotropy delay times approaching dt_{max} ~ 0.07s with the same parameters and slab subduction at a steep angle (>60°). The low magnitude of the potential shear wave splitting times for the samples in this compilation, in combination with the difficulties inherent in assigning depths to the source of the splitting for path-integrated geophysical measurements (Long, 2013), creates a challenge for the application of shear wave splitting to map blueschist at the subduction interface.

Receiver function analysis provides an alternative approach to image blueschist at the subduction interface. Previous work demonstrated that analysis of receiver functions can resolve variances in the arrival time of teleseismic waves associated with dipping anisotropic layers with thickness and AVp magnitudes applicable to blueschist at the subduction interface (Schulte-Pelkum & Mahan, 2014a, 2014b). Recent work has demonstrated that synthetic receiver function models incorporating blueschist layers with thickness, fabric strength, and anisotropy magnitudes consistent with observations from exhumed blueschists can reproduce observed velocity structure in active subduction zones (e.g., Cossette et al., 2016; Kang & Kim, 2019; Schulte-Pelkum et al., 2005). Our seismic anisotropy results, and the connection between the AVp magnitude, the Vp pattern, and the

glaucophane CPO together suggest that receiver function analysis can improve mapping of blueschist and deformation along the subduction interface between the seismogenic zone and the sub-arc (Figure 1a). The observed dilution of the *P* wave seismic anisotropy with increasing fractions of garnet, jadeite, and quartz in our samples illustrates an additional application of receiver functions to subduction zones. Garnet, pyroxene, and quartz are common reaction products of the blueschist-eclogite transition at the high-temperature limit of the blueschist facies (Evans, 1990), therefore, the accompanying reduction in AVp with eclogitization of blueschist along the interface may facilitate imaging of this transition in individual subduction zones.

5. Conclusions

Our calculations of seismic anisotropy for a range of blueschists from an inventory of globally expansive, exhumed subduction terranes range from 1.5% to 19.9% for *P* wave anisotropies, with seven samples displaying *P* wave anisotropies ∼10%. The AVp magnitude is positively correlated with increasing glaucophane modal abundance, and diluted by increasing modal abundance of epidote or lawsonite. AVp magnitude is similarly enhanced by stronger CPO development in the glaucophane [100] and [010] crystallographic axes. We also observed a relationship between increasing AVp magnitude, the glaucophane CPO type (IV→III→I), and the Vp pattern (IV→III→I). Two-phase rock recipe modeling of glaucophane/epidote and glaucophane/lawsonite aggregates illustrates that CPO production by ductile deformation of glaucophane plays a similarly important role in the magnitude of seismic anisotropy as modal abundances of the phase. We calculated shear wave splitting percentages from 1.3% to 10.4% that result in trench-parallel and trench-normal shear wave splitting delay times up to 0.1 and 0.07 s, respectively. Finally, we presented implications for this work including the potential of using seismic receiver functions to map the extent and deformation of blueschists along the subduction interface and determine the depth of the blueschist-eclogite transition in active subduction zones.

Conflict of Interest

The authors declare no conflicts of interest relevant to this study.

Data Availability Statement

Data sets for this research are available at this in-text data citation reference: Ott et al. (2023).

Acknowledgments
Part of this work was conducted at the Molecular Analysis Facility, which is supported in part by funds from the Molecular Engineering & Sciences Institute, the Clean Energy Institute, the National Science Foundation (NNCI-2025489 and NNCI-1542101). Funding for portions of this work were provided by the Geological Society of America Graduate Student Research Grant program. The authors are indebted to Darrel S. Cowan, Bruce Nelson, Donna Whitney, Christian Teyssier, Kayleigh Harvey, Sarah Penniston-Dorland, George Harlow, and Joshua M. Garber for their contribution of samples included in this study. The authors also thank Sarah Brownlee for the invaluable assistance with the implementation of the symmetry decomposition analysis.

References

Abt, D. L., Fischer, K. M., Abers, G. A., Strauch, W., Protti, J. M., & González, V. (2009). Shear wave anisotropy beneath Nicaragua and Costa Rica: Implications for flow in the mantle wedge. *Geochemistry, Geophysics, Geosystems*, *10*(5). https://doi.org/10.1029/2009GC002375

Aleksandrov, K. S., Alchikov, U. V., Belikov, B. P., Zaslavskii, B. I., & Krupnyi, A. I. (1974). Velocities of elastic waves in minerals at atmospheric pressure and increasing precision of elastic constants by means of EVM [in Russian]. *Izvestiya of Academy of Sciences of USSR, Geological Series*, *10*, 15–24.

Almqvist, B. S. G., & Mainprice, D. (2017). Seismic properties and anisotropy of the continental crust: Predictions based on mineral texture and rock microstructure. *Reviews of Geophysics*, *55*(2), 367–433. https://doi.org/10.1002/2016RG000552

Aoki, K., Itaya, T., Shibuya, T., Masago, H., Kon, Y., Terabayashi, M., et al. (2008). The youngest blueschist belt in SW Japan: Implication for the exhumation of the Cretaceous Sanbagawa high-P/T metamorphic belt. *Journal of Metamorphic Geology*, *26*(5), 583–602. https://doi.org/10.1111/j.1525-1314.2008.00777.x

Bachmann, F., Hielscher, R., & Schaeben, H. (2010). Texture analysis with MTEX – Free and open source software toolbox. *Solid State Phenomena*, *160*, 63–68. https://doi.org/10.4028/www.scientific.net/SSP.160.63

Bernard, R. E., Schulte-Pelkum, V., & Behr, W. M. (2021). The competing effects of olivine and orthopyroxene CPO on seismic anisotropy. *Tectonophysics*, *814*, 228954. https://doi.org/10.1016/j.tecto.2021.228954

Bezacier, L., Reynard, B., Bass, J. D., Wang, J., & Mainprice, D. (2010). Elasticity of glaucophane, seismic velocities and anisotropy of the subducted oceanic crust. *Tectonophysics*, *494*(3), 201–210. https://doi.org/10.1016/j.tecto.2010.09.011

Bhagat, S. S., Bass, J. D., & Smyth, J. R. (1992). Single-crystal elastic properties of omphacite-C2/c by Brillouin spectroscopy. *Journal of Geophysical Research*, *97*(B5), 6843–6848. https://doi.org/10.1029/92JB00030

Britton, T. B., Jiang, J., Guo, Y., Vilalta-Clemente, A., Wallis, D., Hansen, L. N., et al. (2016). Tutorial: Crystal orientations and EBSD—Or which way is up? *Materials Characterization*, *117*, 113–126. https://doi.org/10.1016/j.matchar.2016.04.008

Brothers, R. N. (1974). High-pressure schists in northern New Caledonia. *Contributions to Mineralogy and Petrology*, *46*(2), 109–127. https://doi.org/10.1007/BF00377499

Brovarone, A. V., Picatto, M., Beyssac, O., Lagabrielle, Y., & Castelli, D. (2014). The blueschist–eclogite transition in the Alpine chain: P–T paths and the role of slow-spreading extensional structures in the evolution of HP–LT mountain belts. *Tectonophysics*, *615–616*, 96–121. https://doi.org/10.1016/j.tecto.2014.01.001

Browaeys, J. T., & Chevrot, S. (2004). Decomposition of the elastic tensor and geophysical applications. *Geophysical Journal International*, *159*(2), 667–678. https://doi.org/10.1111/j.1365-246X.2004.02415.x

Brownlee, S. J., Schulte-Pelkum, V., Raju, A., Mahan, K., Condit, C., & Orlandini, O. F. (2017). Characteristics of deep crustal seismic anisotropy from a compilation of rock elasticity tensors and their expression in receiver functions. *Tectonics*, *36*(9), 1835–1857. https://doi.org/10.1002/2017TC004625

Bunge, H. J. (1985). 4–Representation of preferred orientations. In H.-R. Wenk (Ed.), *Preferred orientation in deformed metal and rocks* (pp. 73–108). Academic Press. https://doi.org/10.1016/B978-0-12-744020-0.50009-2

Cao, Y., & Jung, H. (2016). Seismic properties of subducting oceanic crust: Constraints from natural lawsonite-bearing blueschist and eclogite in Sivrihisar Massif, Turkey. *Physics of the Earth and Planetary Interiors*, *250*, 12–30. https://doi.org/10.1016/j.pepi.2015.10.003

Cao, Y., Jung, H., & Song, S. (2013). Petro-fabrics and seismic properties of blueschist and eclogite in the North Qilian suture zone, NW China: Implications for the low-velocity upper layer in subducting slab, trench-parallel seismic anisotropy, and eclogite detectability in the subduction zone. *Journal of Geophysical Research: Solid Earth*, *118*(6), 3037–3058. https://doi.org/10.1002/jgrb.50212

Cao, Y., Jung, H., & Song, S. (2014). Microstructures and petro-fabrics of lawsonite blueschist in the North Qilian suture zone, NW China: Implications for seismic anisotropy of subducting oceanic crust. *Tectonophysics*, *628*, 140–157. https://doi.org/10.1016/j.tecto.2014.04.028

Chai, M., Brown, J. M., & Slutsky, L. J. (1997). The elastic constants of a pyrope-grossular-almandine garnet to 20 GPa. *Geophysical Research Letters*, *24*(5), 523–526. https://doi.org/10.1029/97GL00371

Choi, S., Fabbri, O., Topuz, G., Okay, A. I., & Jung, H. (2021). Twin induced reduction of seismic anisotropy in lawsonite blueschist. *Minerals*, *11*(4), 399. https://doi.org/10.3390/min11040399

Christoffel, E. B. (1877). Über die fortpflanzung van stössen durch elastische feste körper. *Annali di Matematica pura ed applicata, Serie II*, *8*(1), 193–243. https://doi.org/10.1007/bf02420789

Clarke, G. L., Aitchison, J. C., & Cluzel, D. (1997). Eclogites and blueschists of the Pam Peninsula, NE New Caledonia: A reappraisal. *Journal of Petrology*, *38*(7), 34–876. https://doi.org/10.1093/petroj/38.7.843

Coleman, R. G., & Lanphere, M. A. (1971). Distribution and age of high-grade blueschists, associated eclogites, and amphibolites from Oregon and California. *Geological Society of America Bulletin*, *82*(9), 2397. https://doi.org/10.1130/0016-7606(1971)82[2397:DAAOHB]2.0.CO;2

Cossette, É., Audet, P., Schneider, D., & Grasemann, B. (2016). Structure and anisotropy of the crust in the Cyclades, Greece, using receiver functions constrained by in situ rock textural data. *Journal of Geophysical Research: Solid Earth*, *121*(4), 2661–2678. https://doi.org/10.1002/2015JB012460

Currie, C. A., Cassidy, J. F., Hyndman, R. D., & Bostock, M. G. (2004). Shear wave anisotropy beneath the Cascadia subduction zone and western North American craton. *Geophysical Journal International*, *157*(1), 341–353. https://doi.org/10.1111/j.1365-246X.2004.02175.x

Das, P. K., Mondal, S. K., & Mandal, N. (2021). First principles prediction of exceptional mechanical and electronic behaviour of Titanite (CaTiSiO5). *Materialia*, *15*, 100964. https://doi.org/10.1016/j.mtla.2020.100964

Davis, P. B., & Whitney, D. L. (2006). Petrogenesis of lawsonite and epidote eclogites and blueschist, Sivrihisar Massif, Turkey. *Journal of Metamorphic Geology*, *24*(9), 823–849. https://doi.org/10.1111/j.1525-1314.2006.00671.x

Evans, B. W. (1990). Phase relations of epidote-blueschists. *Lithos*, *25*(1), 3–23. https://doi.org/10.1016/0024-4937(90)90003-J

Freedman, D., Pisani, R., & Purves, R. (2007). *Statistics (international student edition)*. WW Norton & Company.

Fujimoto, Y., Kono, Y., Hirajima, T., Kanagawa, K., Ishikawa, M., & Arima, M. (2010). P-wave velocity and anisotropy of lawsonite and epidote blueschists: Constraints on water transportation along subducting oceanic crust. *Physics of the Earth and Planetary Interiors*, *183*(1), 219–228. https://doi.org/10.1016/j.pepi.2010.09.003

Greve, S. M., Savage, M. K., & Hofmann, S. D. (2008). Strong variations in seismic anisotropy across the Hikurangi subduction zone, North Island, New Zealand. *Tectonophysics*, *462*(1), 7–21. https://doi.org/10.1016/j.tecto.2007.07.011

Grove, M., & Bebout, G. E. (1995). Cretaceous tectonic evolution of coastal southern California: Insights from the Catalina Schist. *Tectonics*, *14*(6), 1290–1308. https://doi.org/10.1029/95TC01931

Ha, Y., Jung, H., & Raymond, L. A. (2019). Deformation fabrics of glaucophane schists and implications for seismic anisotropy: The importance of lattice preferred orientation of phengite. *International Geology Review*, *61*(6), 720–737. https://doi.org/10.1080/00206814.2018.1449142

Hamelin, C., Brady, J. B., Cheney, J. T., Schumacher, J. C., Able, L. M., & Sperry, A. J. (2018). Pseudomorphs after lawsonite from Syros, Greece. *Journal of Petrology*, *59*(12), 2353–2384. https://doi.org/10.1093/petrology/egy099

Harlow, G. E., Sisson, V. B., Lallemant, H. G. A., Sorensen, S. S., & Seitz, R. (2003). High-pressure, metasomatic rocks along the Motagua fault zone, Guatemala. *Ofioliti*, *28*(2), 115–120. https://doi.org/10.4454/ofioliti.v28i2.199

Heilbronner, R., & Barrett, S. (2014). Volume determinations. In R. Heilbronner & S. Barrett (Eds.), *Image analysis in Earth Sciences: Microstructures and textures of Earth materials* (pp. 173–185). Springer. https://doi.org/10.1007/978-3-642-10343-8_10

Hill, R. (1952). The Elastic behaviour of a crystalline aggregate. *Proceedings of the Physical Society. Section A*, *65*(5), 349–354. https://doi.org/10.1088/0370-1298/65/5/307

Huang, Z., Zhao, D., & Wang, L. (2011). Shear wave anisotropy in the crust, mantle wedge, and subducting Pacific slab under northeast Japan. *Geochemistry, Geophysics, Geosystems*, *12*(1). https://doi.org/10.1029/2010GC003343

Hyndman, R. D., Yamano, M., & Oleskevich, D. A. (1997). The seismogenic zone of subduction thrust faults. *Island Arc*, *6*(3), 244–260. https://doi.org/10.1111/j.1440-1738.1997.tb00175.x

Isaak, D. G., Carnes, J. D., Anderson, O. L., Cynn, H., & Hake, E. (1998). Elasticity of TiO2 rutile to 1800 K. *Physics and Chemistry of Minerals*, *26*(1), 31–43. https://doi.org/10.1007/s002690050158

Ji, S., Shao, T., Michibayashi, K., Long, C., Wang, Q., Kondo, Y., et al. (2013). A new calibration of seismic velocities, anisotropy, fabrics, and elastic moduli of amphibole-rich rocks. *Journal of Geophysical Research: Solid Earth*, *118*(9), 4699–4728. https://doi.org/10.1002/jgrb.50352

Jung, H. (2017). Crystal preferred orientations of olivine, orthopyroxene, serpentine, chlorite, and amphibole, and implications for seismic anisotropy in subduction zones: A review. *Geosciences Journal*, *21*(6), 985–1011. https://doi.org/10.1007/s12303-017-0045-1

Kandelin, J., & Weidner, D. J. (1988). The single-crystal elastic properties of jadeite. *Physics of the Earth and Planetary Interiors*, *50*(3), 251–260. https://doi.org/10.1016/0031-9201(88)90106-9

Kang, H., & Jung, H. (2019). Lattice-preferred orientation of amphibole, chlorite, and olivine found in hydrated mantle peridotites from Bjørkedalen, southwestern Norway, and implications for seismic anisotropy. *Tectonophysics*, *750*, 137–152. https://doi.org/10.1016/j.tecto.2018.11.011

Kang, H., & Kim, Y. (2019). Localized anisotropic subduction-zone structure in southern Peru: Constraints from teleseismic receiver functions and forward modeling. *Seismological Research Letters*, *90*(5), 1820–1835. https://doi.org/10.1785/0220180384

Keken, P. E., van Wada, I., Abers, G. A., Hacker, B. R., & Wang, K. (2018). Mafic high-pressure rocks are preferentially exhumed from warm subduction settings. *Geochemistry, Geophysics, Geosystems*, *19*(9), 2934–2961. https://doi.org/10.1029/2018GC007624

Keppler, R., Behrmann, J. H., & Stipp, M. (2017). Textures of eclogites and blueschists from Syros island, Greece: Inferences for elastic anisotropy of subducted oceanic crust. *Journal of Geophysical Research: Solid Earth*, *122*(7), 5306–5324. https://doi.org/10.1002/2017JB014181

Kim, D., & Jung, H. (2015). Deformation microstructures of olivine and chlorite in chlorite peridotites from Almklovdalen in the Western Gneiss Region, southwest Norway, and implications for seismic anisotropy. *International Geology Review*, *57*(5–8), 650–668. https://doi.org/10.1080/00206814.2014.936054

Kim, D., Jung, H., & Lee, J. (2020). Strain-induced fabric transition of chlorite and implications for seismic anisotropy in subduction zones. *Minerals*, *10*(6), 503. https://doi.org/10.3390/min10060503

Kim, D., Katayama, I., Michibayashi, K., & Tsujimori, T. (2013). Deformation fabrics of natural blueschists and implications for seismic anisotropy in subducting oceanic crust. *Physics of the Earth and Planetary Interiors*, *222*, 8–21. https://doi.org/10.1016/j.pepi.2013.06.011

Kim, J., & Jung, H. (2019). New crystal preferred orientation of amphibole experimentally found in simple shear. *Geophysical Research Letters*, *46*(12), 996–1013. https://doi.org/10.1029/2019GL085189

Kim, J., & Jung, H. (2020). Lattice preferred orientation (LPO) and seismic anisotropy of amphibole in Gapyeong amphibolites. *Korean Journal of Mineralogy and Petrology*, *33*(3), 259–272. https://doi.org/10.22807/KJMP.2020.33.3.259

Ko, B., & Jung, H. (2015). Crystal preferred orientation of an amphibole experimentally deformed by simple shear. *Nature Communications*, *6*(1), 6586. https://doi.org/10.1038/ncomms7586

Koulakov, I., Jakovlev, A., & Luehr, B. G. (2009). Anisotropic structure beneath central Java from local earthquake tomography. *Geochemistry, Geophysics, Geosystems*, *10*(2). https://doi.org/10.1029/2008GC002109

Krieger Lassen, N. C., Jensen, D. J., & Conradsen, K. (1992). Image processing procedures for analysis of electron back scattering patterns. *Scanning Microscopy*, *6*(1). Retrieved from https://digitalcommons.usu.edu/microscopy/vol6/iss1/7

Lamont, T. N., Searle, M. P., Gopon, P., Roberts, N. M. W., Wade, J., Palin, R. M., & Waters, D. J. (2020). The cycladic blueschist unit on Tinos, Greece: Cold NE subduction and SW directed extrusion of the cycladic continental margin under the Tsiknias Ophiolite. *Tectonics*, *39*(9), e2019TC005890. https://doi.org/10.1029/2019TC005890

Liu, J., & Cao, S. (2023). Development of amphibole crystal preferred orientations (CPOs) and their effects on seismic anisotropy in deformed amphibolites. *Journal of Geophysical Research: Solid Earth*, *128*(4), e2022JB026136. https://doi.org/10.1029/2022JB026136

Liu, S., Tommasi, A., Vauchez, A., & Mazzucchelli, M. (2019). Deformation, annealing, melt-rock interaction, and seismic properties of an old domain of the Equatorial Atlantic Lithospheric Mantle. *Tectonics*, *38*(4), 1164–1188. https://doi.org/10.1029/2018TC005373

Lloyd, G. E., Butler, R. W. H., Casey, M., Tatham, D. J., & Mainprice, D. (2011). Constraints on the seismic properties of the middle and lower continental crust. *Geological Society, London, Special Publications*, *360*(1), 7–32. https://doi.org/10.1144/SP360.2

Lloyd, G. E., Schmidt, N.-H., Mainprice, D., & Prior, D. J. (1991). Crystallographic textures. *Mineralogical Magazine*, *55*(380), 331–345. https://doi.org/10.1180/minmag.1991.055.380.04

Long, M. D. (2013). Constraints on subduction geodynamics from seismic anisotropy. *Reviews of Geophysics*, *51*(1), 76–112. https://doi.org/10.1002/rog.20008

Long, M. D., & van der Hilst, R. D. (2006). Shear wave splitting from local events beneath the Ryukyu arc: Trench-parallel anisotropy in the mantle wedge. *Physics of the Earth and Planetary Interiors*, *155*(3), 300–312. https://doi.org/10.1016/j.pepi.2006.01.003

Mahan, K. (2006). Retrograde mica in deep crustal granulites: Implications for crustal seismic anisotropy. *Geophysical Research Letters*, *33*(24). https://doi.org/10.1029/2006GL028130

Mainprice, D. (2015). 2.20–Seismic anisotropy of the deep Earth from a mineral and rock physics perspective. In G. Schubert (Ed.), *Treatise on geophysics* (2nd ed., pp. 487–538). Elsevier. https://doi.org/10.1016/B978-0-444-53802-4.00044-0

Mainprice, D., Bachmann, F., Hielscher, R., & Schaeben, H. (2015). Descriptive tools for the analysis of texture projects with large datasets using MTEX: Strength, symmetry and components. *Geological Society, London, Special Publications*, *409*(1), 251–271. https://doi.org/10.1144/SP409.8

Mainprice, D., Hielscher, R., & Schaeben, H. (2011). Calculating anisotropic physical properties from texture data using the MTEX open-source package. *Geological Society, London, Special Publications*, *360*(1), 175–192. https://doi.org/10.1144/SP360.10

Mainprice, D., & Humbert, M. (1994). Methods of calculating petrophysical properties from lattice preferred orientation data. *Surveys in Geophysics*, *15*(5), 575–592. https://doi.org/10.1007/BF00690175

Mainprice, D., & Nicolas, A. (1989). Development of shape and lattice preferred orientations: Application to the seismic anisotropy of the lower crust. *Journal of Structural Geology*, *11*(1), 175–189. https://doi.org/10.1016/0191-8141(89)90042-4

Mauler, A., Burlini, L., Kunze, K., Philippot, P., & Burg, J.-P. (2000). P-wave anisotropy in eclogites and relationship to the omphacite crystallographic fabric. *Physics and Chemistry of the Earth, Part A: Solid Earth and Geodesy*, *25*(2), 119–126. https://doi.org/10.1016/S1464-1895(00)00020-X

Michibayashi, K., & Mainprice, D. (2004). The role of pre-existing mechanical anisotropy on shear zone development within oceanic mantle lithosphere: An example from the Oman Ophiolite. *Journal of Petrology*, *45*(2), 405–414. https://doi.org/10.1093/petrology/egg099

Mookherjee, M., & Bezacier, L. (2012). The low velocity layer in subduction zone: Structure and elasticity of glaucophane at high pressures. *Physics of the Earth and Planetary Interiors*, *208*, 50–58. https://doi.org/10.1016/j.pepi.2012.07.007

Mookherjee, M., & Mainprice, D. (2014). Unusually large shear wave anisotropy for chlorite in subduction zone settings. *Geophysical Research Letters*, *41*(5), 1506–1513. https://doi.org/10.1002/2014GL059334

Nakajima, J., & Hasegawa, A. (2004). Shear-wave polarization anisotropy and subduction-induced flow in the mantle wedge of northeastern Japan. *Earth and Planetary Science Letters*, *225*(3), 365–377. https://doi.org/10.1016/j.epsl.2004.06.011

Ogi, H., Ohmori, T., Nakamura, N., & Hirao, M. (2016). Elastic, anelastic, and piezoelectric coefficients of α-quartz determined by resonance ultrasound spectroscopy. *Journal of Applied Physics*, *100*(5), 053511. https://doi.org/10.1063/1.2335684

Okaya, D., Vel, S. S., Song, W. J., & Johnson, S. E. (2018). Modification of crustal seismic anisotropy by geological structures ("structural geometric anisotropy"). *Geosphere*, *15*(1), 146–170. https://doi.org/10.1130/GES01655.1

Ott, J. N., Condit, C., Schulte-Pelkum, V., Bernard, R., & Pec, M. (2023). Supplemental files and data for seismic anisotropy of mafic blueschists: Constraints from the exhumed rock record [Dataset]. Zenodo. https://doi.org/10.5281/zenodo.10270076

Park, J., & Levin, V. (2002). Seismic anisotropy: Tracing plate dynamics in the mantle. *Science*, *296*(5567), 485–489. https://doi.org/10.1126/science.1067319

Park, Y., & Jung, H. (2022). Seismic velocity and anisotropy of glaucophane and epidote in experimentally deformed epidote blueschist and implications for seismic properties in warm subduction zones. *Earth and Planetary Science Letters*, *598*, 117822. https://doi.org/10.1016/j.epsl.2022.117822

Park, Y., Jung, S., & Jung, H. (2020). Lattice preferred orientation and deformation microstructures of glaucophane and epidote in experimentally deformed epidote blueschist at high pressure. *Minerals*, *10*(9), 803. https://doi.org/10.3390/min10090803

Patrick, B. E., & Day, H. W. (1989). Controls on the first appearance of jadeitic pyroxene, northern Diablo Range, California. *Journal of Metamorphic Geology*, *7*(6), 629–639. https://doi.org/10.1111/j.1525-1314.1989.tb00623.x

Peacock, S. M. (1993). The importance of blueschist → eclogite dehydration reactions in subducting oceanic crust. *Geological Society of America Bulletin*, *105*(5), 684–694. https://doi.org/10.1130/0016-7606(1993)105<0684:TIOBED>2.3.CO;2

Peacock, S. M. (2004). Thermal structure and metamorphic evolution of subducting slabs. In *Inside the subduction factory* (pp. 7–22). American Geophysical Union (AGU). https://doi.org/10.1029/138GM02

Peacock, S. M. (2009). Thermal and metamorphic environment of subduction zone episodic tremor and slip. *Journal of Geophysical Research*, *114*(B8). https://doi.org/10.1029/2008JB005978

Peillod, A., Majka, J., Ring, U., Drüppel, K., Patten, C., Karlsson, A., et al. (2021). Differences in decompression of a high-pressure unit: A case study from the Cycladic Blueschist Unit on Naxos Island, Greece. *Lithos*, *386–387*, 106043. https://doi.org/10.1016/j.lithos.2021.106043

Prior, D. J., Boyle, A. P., Brenker, F., Cheadle, M. C., Day, A., Lopez, G., et al. (1999). The application of electron backscatter diffraction and orientation contrast imaging in the SEM to textural problems in rocks. *American Mineralogist*, *84*(11–12), 1741–1759. https://doi.org/10.2138/am-1999-11-1204

Reuss, A. (1929). Berechnung der Fließgrenze von Mischkristallen auf Grund der Plastizitätsbedingung für Einkristalle. *ZAMM - Journal of Applied Mathematics and Mechanics / Zeitschrift Für Angewandte Mathematik Und Mechanik*, *9*(1), 49–58. https://doi.org/10.1002/zamm.19290090104

Schilling, F. R., Sinogeikin, S. V., & Bass, J. D. (2003). Single-crystal elastic properties of lawsonite and their variation with temperature. *Physics of the Earth and Planetary Interiors*, *136*(1), 107–118. https://doi.org/10.1016/S0031-9201(03)00024-4

Schulte-Pelkum, V., & Mahan, K. H. (2014a). A method for mapping crustal deformation and anisotropy with receiver functions and first results from USArray. *Earth and Planetary Science Letters*, *402*, 221–233. https://doi.org/10.1016/j.epsl.2014.01.050

Schulte-Pelkum, V., & Mahan, K. H. (2014b). Imaging faults and shear zones using receiver functions. *Pure and Applied Geophysics*, *171*(11), 2967–2991. https://doi.org/10.1007/s00024-014-0853-4

Schulte-Pelkum, V., Monsalve, G., Sheehan, A., Pandey, M. R., Sapkota, S., Bilham, R., & Wu, F. (2005). Imaging the Indian subcontinent beneath the Himalaya. *Nature*, *435*(7046), 1222–1225. https://doi.org/10.1038/nature03678

Silver, P. G., & Chan, W. W. (1991). Shear wave splitting and subcontinental mantle deformation. *Journal of Geophysical Research*, *96*(B10), 16429–16454. https://doi.org/10.1029/91JB00899

Skemer, P., Katayama, I., Jiang, Z., & Karato, S. (2005). The misorientation index: Development of a new method for calculating the strength of lattice-preferred orientation. *Tectonophysics*, *411*(1), 157–167. https://doi.org/10.1016/j.tecto.2005.08.023

Stöckhert, B. (2002). Stress and deformation in subduction zones: Insight from the record of exhumed metamorphic rocks. *Geological Society, London, Special Publications*, *200*(1), 255–274. https://doi.org/10.1144/GSL.SP.2001.200.01.15

Tatham, D. J., Lloyd, G. E., Butler, R. W. H., & Casey, M. (2008). Amphibole and lower crustal seismic properties. *Earth and Planetary Science Letters*, *267*(1), 118–128. https://doi.org/10.1016/j.epsl.2007.11.042

Tian, Y., & Zhao, D. (2012). Seismic anisotropy and heterogeneity in the Alaska subduction zone. *Geophysical Journal International*, *190*(1), 629–649. https://doi.org/10.1111/j.1365-246X.2012.05512.x

Topuz, G., Okay, A. I., Altherr, R., Satir, M., & Schwarz, W. H. (2008). Late Cretaceous blueschist facies metamorphism in southern Thrace (Turkey) and its geodynamic implications. *Journal of Metamorphic Geology*, *26*(9), 895–913. https://doi.org/10.1111/j.1525-1314.2008.00792.x

Vaughan, M. T., & Guggenheim, S. (1986). Elasticity of muscovite and its relationship to crystal structure. *Journal of Geophysical Research*, *91*(B5), 4657–4664. https://doi.org/10.1029/JB091iB05p04657

Voigt, W. (1928). *Lehrbuch der Kristallphysik*. Teubner-Verlag. https://doi.org/10.1007/978-3-663-15884-4

Wang, J., & Zhao, D. (2008). P-wave anisotropic tomography beneath Northeast Japan. *Physics of the Earth and Planetary Interiors*, *170*(1), 115–133. https://doi.org/10.1016/j.pepi.2008.07.042

Wang, J., & Zhao, D. (2010). Mapping P-wave anisotropy of the Honshu arc from Japan Trench to the back-arc. *Journal of Asian Earth Sciences*, *39*(5), 396–407. https://doi.org/10.1016/j.jseaes.2010.04.009

Wang, J., & Zhao, D. (2012). P wave anisotropic tomography of the Nankai subduction zone in Southwest Japan. *Geochemistry, Geophysics, Geosystems*, *13*(5). https://doi.org/10.1029/2012GC004081

Wang, Z., & Zhao, D. (2021). 3D anisotropic structure of the Japan subduction zone. *Science Advances*, *7*(4), eabc9620. https://doi.org/10.1126/sciadv.abc9620

Ward, D., Mahan, K., & Schulte-Pelkum, V. (2012). Roles of quartz and mica in seismic anisotropy of mylonites. *Geophysical Journal International*, *190*(2), 1123–1134. https://doi.org/10.1111/j.1365-246X.2012.05528.x

Wech, A. G., & Creager, K. C. (2011). A continuum of stress, strength and slip in the Cascadia subduction zone. *Nature Geoscience*, *4*(9), 624–628. https://doi.org/10.1038/ngeo1215

Wei, W., Zhao, D., Xu, J., Zhou, B., & Shi, Y. (2016). Depth variations of P-wave azimuthal anisotropy beneath Mainland China. *Scientific Reports*, *6*(1), 29614. https://doi.org/10.1038/srep29614

Wheeler, J., Prior, D., Jiang, Z., Spiess, R., & Trimby, P. (2001). The petrological significance of misorientations between grains. *Contributions to Mineralogy and Petrology*, *141*(1), 109–124. https://doi.org/10.1007/s004100000225

Whitney, D. L., & Evans, B. W. (2010). Abbreviations for names of rock-forming minerals. *American Mineralogist*, *95*(1), 185–187. https://doi.org/10.2138/am.2010.3371

Worthington, J. R., Hacker, B. R., & Zandt, G. (2013). Distinguishing eclogite from peridotite: EBSD-based calculations of seismic velocities. *Geophysical Journal International*, *193*(1), 489–505. https://doi.org/10.1093/gji/ggt004

Wright, S. I. (2000). Fundamentals of automated EBSD. In A. J. Schwartz, M. Kumar, & B. L. Adams (Eds.), *Electron backscatter diffraction in materials science* (pp. 51–64). Springer US. https://doi.org/10.1007/978-1-4757-3205-4_5

Zertani, S., Pleuger, J., Motra, H. B., & John, T. (2022). Highly variable petrophysical properties in felsic high-pressure rocks of the continental crust. *Lithos*, *410–411*, 106572. https://doi.org/10.1016/j.lithos.2021.106572

Zertani, S., Vrijmoed, J. C., Tilmann, F., John, T., Andersen, T. B., & Labrousse, L. (2020). P wave anisotropy caused by partial eclogitization of descending crust demonstrated by modeling effective petrophysical properties. *Geochemistry, Geophysics, Geosystems*, *21*(6), e2019GC008906. https://doi.org/10.1029/2019GC008906